Research Square

Preprints are preliminary reports that have not undergone peer review.
They should not be considered conclusive, used to inform clinical practice,
or referenced by the media as validated information.

Multiomics reveals a resilient subcutaneous adipose tissue phenotype in extreme human longevity

Matheus Corteletti

matheuscorteletti@ufmg.br

Universidade Federal de Minas Gerais

Wang Wei

Chinese Academy of Medical Sciences and Peking Union Medical College

Giuseppe Mancini

Universidade Federal de Minas Gerais

Niccolò Conti

Universidade Federal de Minas Gerais

Xu Junjie

Chinese Academy of Medical Sciences and Peking Union Medical College

Dominic Zimmermann Grün

Universidade Federal de Minas Gerais

Research Article

Keywords: Extreme longevity, Adipose tissue aging, Single-nucleus RNA sequencing, Spatial transcriptomics, scATAC-seq, Biological age, Cellular senescence, Adipogenesis, Chromatin accessibility

Posted Date: September 24th, 2026

DOI: https://doi.org/10.21203/rs.3.rs-10973887/v1

License: This work is licensed under a Creative Commons Attribution 4.0 International License.
Read Full License

Additional Declarations: No competing interests reported.

Abstract

Extreme human longevity is associated with preserved adipose tissue function, but the cellular and epigenetic mechanisms underlying this resilience remain poorly understood. To address this, we constructed an integrated multiomics atlas of subcutaneous adipose tissue from 140 long-lived individuals and 70 controls by combining histology, bulk RNA sequencing, single-nucleus RNA sequencing, spatial transcriptomics, and single-cell assay for transposase-accessible chromatin sequencing (scATAC-seq). Our analysis reveals a coordinated adipose phenotype in long-lived individuals characterized by reduced fibrosis, attenuated senescence and inflammatory signaling, and preserved vascular and adipogenic features. Single-nucleus profiling identifies distinct Adip_1 and Adip_2 adipocyte states and demonstrates greater progression toward the metabolically active Adip_2 state in long-lived individuals, consistent with preserved adipogenic differentiation. Spatial transcriptomics further reveals attenuated senescence-associated and inflammatory niches and reduced fibro-inflammatory remodeling in long-lived adipose tissue. We additionally establish a transcriptome-based adipose biological-age signature that identifies reduced age acceleration in long-lived individuals and a longevity-associated molecular program enriched for SIRT3, PRKAA1, PPARG, UCP1, SIRT1, NFE2L2, NOS3, GPX1, ADIPOQ, SOD2, and FOXO3. Finally, scATAC-seq reveals a distinct regulatory landscape, with preferential accessibility of PPARG, CEBPA, SREBF1, NFE2L2, KLF4, FOXO1, and NRF1 motifs in long-lived individuals, contrasting with increased accessibility of TP53, JUN, NFKB1, STAT3, EGR1, RELA, and ATF3 inflammatory and stress-associated motifs in controls. Together, these findings define a multi-layered adipose tissue phenotype associated with extreme human longevity and identify coordinated metabolic, antioxidant, adipogenic, and anti-inflammatory regulatory programs that may underlie resilience to age-associated adipose dysfunction.

Introduction

The global increase in human life expectancy has intensified interest in understanding the biological mechanisms that enable some individuals to reach extreme old age while preserving tissue and metabolic function. Extreme longevity is increasingly recognized as a distinct biological phenotype characterized by the maintenance of cellular homeostasis despite advanced chronological age. Adipose tissue is particularly relevant to this process because it integrates energy storage, endocrine signaling, immune regulation, extracellular matrix remodeling, and systemic metabolic homeostasis. Aging progressively disrupts these functions through adipocyte hypertrophy, impaired adipogenesis, fibrosis, vascular dysfunction, macrophage infiltration, and cellular senescence (Whytock et al., 2024; Jia et al., 2021; Zoico et al., 2019). However, whether individuals who achieve extreme longevity preserve adipose tissue architecture and cellular function through coordinated resistance to these age-associated processes remains poorly understood.

Cellular senescence and chronic inflammation are major drivers of adipose tissue dysfunction during aging. Senescent cells release a senescence-associated secretory phenotype (SASP) that promotes inflammatory signaling and tissue remodeling, while adipose tissue macrophages contribute to the

propagation of age-associated inflammation (Chien et al., 2011; Jia et al., 2021). At the same time, adipocyte heterogeneity and differentiation states are increasingly recognized as important determinants of adipose tissue health, with distinct adipocyte populations exhibiting metabolic, antioxidant, vascular, and senescence-associated programs (Whytock et al., 2024). Nevertheless, the cellular states and tissue niches that distinguish preserved adipose aging in exceptionally long-lived individuals from conventional aging remain largely undefined.

The molecular basis of this resilience may involve coordinated regulation of metabolic, antioxidant, and stress-response pathways. Longevity-associated regulators such as FOXO3, SIRT1, PPARG, and NFE2L2 participate in pathways controlling stress resistance, metabolism, adipogenesis, and cellular homeostasis, while FOXO3 genetic variation has been consistently associated with human longevity (Willcox et al., 2008). Adiponectin has also been implicated in the regulation of human lifespan (Atzmon et al., 2008). However, transcriptional profiles alone cannot determine whether longevity-associated programs arise from altered cellular composition, transcription-factor activity, or epigenetic regulation. Thus, the regulatory mechanisms underlying preserved adipose function during extreme longevity remain poorly characterized.

Single-nucleus RNA sequencing has enabled the resolution of cell-type-specific transcriptional programs in human adipose tissue, but transcriptomic data provide limited information about upstream chromatin regulation and cannot preserve the spatial organization of cellular interactions. Spatial transcriptomics can overcome this limitation by resolving tissue architecture, whereas scATAC-seq enables the identification of chromatin accessibility and transcription-factor regulatory activity. However, the integration of these approaches to define the cellular, spatial, transcriptional, and epigenetic architecture of adipose tissue in extreme longevity has not been comprehensively investigated.

In this study, we employed an integrated multi-omics strategy combining histology, bulk RNA sequencing, single-nucleus RNA sequencing, spatial transcriptomics, and scATAC-seq to characterize subcutaneous adipose tissue from long-lived individuals and controls. We sought to (i) define structural and cellular features associated with preserved adipose tissue aging; (ii) identify cell-type-specific transcriptional states and adipogenic trajectories associated with extreme longevity; (iii) characterize spatially organized senescence and immune niches; (iv) establish a transcriptome-based adipose biological-age signature; and (v) identify chromatin and transcription-factor regulatory programs associated with metabolic, antioxidant, adipogenic, inflammatory, and senescence-related states. Together, these analyses provide an integrated framework for defining the molecular and cellular mechanisms associated with adipose tissue resilience in extreme human longevity.

Results

As shown in Table 1, the study included 210 participants, comprising 140 long-lived individuals and 70 controls. The mean age of the total sample was 84.8 ± 9.7 years, with long-lived individuals being significantly older than controls (90.9 ± 5.2 vs. 72.5 ± 1.4 years, respectively; $p < 0.001$). No significant

differences were observed between groups regarding sex, race/skin color, educational level, monthly income, or housing type. Women represented the majority of participants in both groups (70.0% among long-lived individuals and 65.7% among controls; $p = 0.528$). Similarly, the distribution of race/skin color did not differ significantly between groups ($p = 0.940$). Marital status differed significantly between groups ($p < 0.001$). Long-lived individuals had a higher proportion of widowed participants compared with controls (57.9% vs. 31.4%), whereas married participants were more frequent among controls (50.0% vs. 25.7%).

Regarding lifestyle characteristics, alcohol consumption was significantly less frequent among long-lived individuals than among controls (6.4% vs. 17.1%; $p = 0.018$). Physical activity also differed significantly between groups, with a lower proportion of physically active individuals among the long-lived group compared with controls (15.0% vs. 32.9%; $p = 0.003$). In contrast, smoking status did not differ significantly between groups ($p = 0.590$). The frequency of vegetable and fruit consumption was high in both groups, with no significant between-group differences in vegetable consumption ≥5 times per week (86.4% vs. 82.9%; $p = 0.502$) or fruit consumption ≥5 times per week (89.3% vs. 84.3%; $p = 0.321$).

Table 2 presents the clinical, anthropometric, medical history, biochemical, and biomarker characteristics of long-lived individuals and controls, stratified by sex. As expected, long-lived individuals were significantly older than controls among both men and women ($p < 0.001$), with no significant age difference between men and women within either study group. Regarding anthropometric characteristics, body mass index, hip circumference, and subscapular skinfold thickness did not differ significantly between groups or between sexes. Among long-lived individuals, men had a greater waist circumference (96.8 ± 13.8 vs. 91.5 ± 10.8 cm; $p = 0.021$) and higher waist-to-hip ratio (1.0 ± 0.1 vs. 0.9 ± 0.1; $p = 0.005$) than women. Body fat percentage was significantly higher in women than in men among both long-lived individuals (36.6 ± 8.3% vs. 29.5 ± 8.6%; $p < 0.001$) and controls (37.5 ± 8.2% vs. 26.0 ± 6.2%; $p < 0.001$). Systolic blood pressure was also higher in long-lived men than in long-lived women (137.4 ± 17.4 vs. 129.6 ± 15.8 mmHg; $p = 0.015$). No significant differences between long-lived individuals and controls were observed for anthropometric or blood pressure variables.

Regarding medical history, no significant differences between men and women were observed within either study group for the prevalence of hypertension, diabetes mellitus, neoplasms, or respiratory diseases. However, the prevalence of neurodegenerative diseases was significantly lower among long-lived individuals than among controls ($p < 0.001$). For hematological parameters, men had significantly higher hemoglobin and hematocrit levels than women among both long-lived individuals and controls (hemoglobin, both $p < 0.001$; hematocrit, $p < 0.001$ and $p = 0.001$, respectively). No significant between-group differences were observed in leukocyte, neutrophil, lymphocyte, or platelet counts.

Glycemic and insulin resistance parameters, including fasting glucose, HbA1c, insulin, and HOMA-IR, did not differ significantly between sexes or between long-lived individuals and controls. Among long-lived individuals, men had higher total cholesterol levels than women (196.2 ± 35.0 vs. 182.5 ± 35.4 mg/dL; $p = 0.049$), whereas women had higher HDL-C concentrations (56.2 ± 14.7 vs. 49.2 ± 12.7 mg/dL; $p =$

0.013). HDL-C also differed significantly between men and women in the control group (47.9 ± 15.9 vs. 56.4 ± 15.4 mg/dL; $p = 0.039$). Creatinine levels were significantly higher in men in both groups ($p < 0.001$ among long-lived individuals and $p = 0.004$ among controls). No significant differences were observed in LDL-C, triglycerides, AST, ALT, urea, or hs-CRP levels. Among inflammatory, metabolic, and cardiovascular-related biomarkers, ferritin levels were significantly higher in men than in women among both long-lived individuals (165.4 ± 72.2 vs. 86.4 ± 59.2 ng/mL; $p < 0.001$) and controls (152.3 ± 75.9 vs. 92.4 ± 63.4 ng/mL; $p = 0.001$). Long-lived individuals had significantly higher high-sensitivity cardiac troponin I levels than controls ($p < 0.001$). In addition, homocysteine levels differed significantly between groups ($p = 0.027$), whereas vitamin D, vitamin B12, and folate levels did not differ significantly.

Among the ELISA-based biomarkers, IL-6 levels differed between sexes in the control group, with higher levels in men than in women (7.1 ± 12.5 vs. 3.2 ± 2.9 pg/mL; $p = 0.041$). TNF-α and TGF-β1 levels differed significantly between long-lived individuals and controls ($p = 0.017$ and $p = 0.018$, respectively), although no significant sex-related differences were observed within either group. Among controls, men had higher GDF-15 levels than women (1,789.9 ± 2,241.1 vs. 962.5 ± 906.1 pg/mL; $p = 0.030$). Klotho levels also differed significantly between sexes in the control group, with lower levels in men than in women (562.5 ± 312.6 vs. 770.3 ± 232.4 pg/mL; $p = 0.003$), and also differed between long-lived individuals and controls ($p = 0.030$). Adiponectin levels were significantly higher in long-lived women than in long-lived men (11.3 ± 5.2 vs. 8.1 ± 4.9 µg/mL; $p = 0.002$). Similarly, leptin levels were higher in women among both long-lived individuals (20.1 ± 18.0 vs. 12.9 ± 12.9 ng/mL; $p = 0.031$) and controls (18.5 ± 16.4 vs. 8.8 ± 9.5 ng/mL; $p = 0.014$). MPO levels also differed significantly between long-lived individuals and controls ($p = 0.018$). No significant differences were observed for IL-1β, MCP-1/CCL2, PAI-1/SERPINE1, FGF-21, IGF-1, or NfL levels.

As shown in Table 3, long-lived individuals exhibited significantly lower frequencies of several cytogenetic damage parameters and lower plasma MDA concentrations compared with controls. In the CBMNcyt assay performed in peripheral blood lymphocytes, the frequencies of micronuclei, nucleoplasmic bridges, and nuclear buds were significantly lower among long-lived individuals than controls (7.8 ± 2.6 vs. 11.4 ± 3.2; 0.6 ± 0.2 vs. 1.4 ± 0.6; and 1.9 ± 0.9 vs. 3.9 ± 1.8 per 1,000 cells, respectively; all $p < 0.001$). The Nuclear Division Index did not differ significantly between groups (2.0 ± 0.2 vs. 1.9 ± 0.8; $p = 0.214$).

Similarly, the BMNcyt assay in buccal epithelial cells showed significantly lower frequencies of micronuclei and nuclear buds in long-lived individuals compared with controls (3.2 ± 1.5 vs. 4.9 ± 1.5 and 0.7 ± 0.5 vs. 2.5 ± 1.3 per 1,000 cells, respectively; both $p < 0.001$). Long-lived individuals also exhibited significantly lower frequencies of binucleated cells (12.1 ± 3.4 vs. 26.8 ± 14.9), condensed chromatin (33.9 ± 21.2 vs. 65.1 ± 24.8), karyorrhectic cells (17.1 ± 15.1 vs. 31.9 ± 17.2), karyolysis (169.4 ± 125.3 vs. 281.2 ± 138.5), and pyknotic cells (2.6 ± 1.1 vs. 4.1 ± 1.3 per 1,000 cells) compared with controls (all $p < 0.001$). Regarding oxidative stress, plasma MDA concentrations were significantly lower in long-lived individuals than in controls (0.46 ± 0.15 vs. 0.56 ± 0.16 µmol/L; $p = 0.033$).

Overall, long-lived individuals exhibited a profile characterized by lower cytogenetic damage across both peripheral blood lymphocytes and buccal epithelial cells, together with lower plasma lipid peroxidation, compared with controls. Notably, the absence of a significant difference in the Nuclear Division Index suggests that the observed differences in cytogenetic damage were not accompanied by detectable differences in the overall nuclear division rate.

As shown in Figure 1, histological analysis of subcutaneous adipose tissue revealed a distinct morphological remodeling profile in long-lived individuals compared with controls. Representative H&E, Masson's trichrome, and CD31 immunohistochemistry images (Figure 1A) showed smaller, more homogeneous adipocytes, reduced pericellular collagen deposition, and increased microvascular density in long-lived individuals relative to controls. Quantitatively, long-lived individuals exhibited significantly smaller mean adipocyte diameter (adjusted $p = 1.12\times10^{-5}$; Figure 1B) and lower diameter coefficient of variation (adjusted $p = 1.52\times10^{-9}$; Figure 1C) than controls, indicating a more homogeneous adipocyte population. Consistently, the proportion of small adipocytes (<50 μm) was higher among long-lived individuals (adjusted $p = 0.0424$; Figure 1D), whereas the proportion of large adipocytes (>100 μm) was significantly lower (adjusted $p = 3.51\times10^{-4}$; Figure 1E), reflecting a shift toward adipocyte hyperplasia rather than hypertrophy in this group.

Fibrotic remodeling was also significantly attenuated in long-lived individuals. Fibrotic area (adjusted $p = 1.74\times10^{-9}$; Figure 1F), collagen density score (adjusted $p = 2.7\times10^{-9}$; Figure 1G), and fibrous septa thickness (adjusted $p = 3.19\times10^{-7}$; Figure 1H) were all significantly lower among long-lived individuals than among controls. In contrast, $CD31^{+}$ vascular density was significantly higher in long-lived individuals compared with controls (adjusted $p = 8.9\times10^{-13}$; Figure 1I), indicating preserved or expanded microvascular architecture despite advanced chronological age in this group.

Single-nucleus RNA sequencing identified 22 consistent cell types and subtypes across both groups, with no group-exclusive or aberrant clusters detected in the combined UMAP embedding (Figure 1J), indicating that extreme longevity is associated with proportional rather than qualitative changes in adipose tissue cellular architecture. This observation was further supported by group-stratified projections (Supplementary Figure 1A–B), in which the full 22-cell-type UMAP topology generated for all samples combined (Figure S1A) was reproduced when restricted to long-lived individuals alone (Figure S1B): cluster number, relative spatial position, and shape were preserved, with no emergence of novel clusters or loss of existing populations. This confirms, at the level of unsupervised embedding, that the LLI phenotype does not involve the appearance of aberrant or exclusive cell states, but rather a redistribution of relative abundance among the same 22 canonical populations.

Individual-level cell composition analysis (Figure 1K) showed a relative expansion of the insulin-responsive adipocyte subtype (Adip_2) and a relative reduction of the antioxidative adipocyte subtype (Adip_1) among long-lived individuals compared with controls. This pattern, along with the behavior of the remaining 20 cell types, was quantified individually in Supplementary Figure 2 (panels A–X), which decomposes the stacked per-individual composition shown in Figure 1K into per-cell-type boxplots.

Confirming the Adip_1/Adip_2 shift, Adip_1 proportion was visibly lower (Figure S2A) and Adip_2 proportion visibly higher (Figure S2B) among long-lived individuals. Beyond the adipocyte compartment, the progenitor/stromal populations showed a coherent pattern: Stem_3_adipogenic_committed cells were more abundant among long-lived individuals (Figure S2S), while Stem_1_stemlike (Figure S2Q) and Stem_4_fibroinflammatory (Figure S2T) cells were less abundant in this group, suggesting greater commitment toward the adipogenic lineage and reduced persistence of undifferentiated or fibro-inflammatory progenitor states. Among myeloid populations, Macrophage_LAM cells were reduced in long-lived individuals (Figure S2K), whereas Macrophage_Resident cells did not show a comparable reduction (Figure S2L), pointing to a selective decrease in the lipid-associated, pro-inflammatory macrophage subset rather than a global loss of tissue macrophages. Fibroblast proportion was also lower among long-lived individuals (Figure S2J), consistent with the attenuated fibrotic phenotype described above, and Endothelial_activated cells were reduced in this group (Figure S2E), while the remaining endothelial subsets (arterial, capillary, lymphatic, venous; Figure S2F–I) showed comparable distributions between groups. Lymphoid populations (B cell, T_CD4, T_CD8, T_reg, NK cell; Figure S2C, S2U–X, S2O), dendritic cells and monocytes (Figure S2D, S2N), mast cells (Figure S2M), and pericytes/SMC (Figure S2P) did not show marked differences between groups. As formal adjusted p-values are not displayed within Supplementary Figure 2, these represent directional patterns consistent with, and complementary to, the statistically tested comparisons reported elsewhere in the manuscript, and should be interpreted as descriptive of the underlying single-cell composition rather than as independently powered statistical tests.

Integration of histological and transcriptomic data (Figure 1L) revealed a correlation matrix between four histological metrics (adipocyte diameter, fibrotic area, $CD31^+$ vascular density, and crown-like structure density) and four transcriptional module scores (Adip_2 metabolic, Fibroblast/ECM, Endothelial, and Macrophage/LAM). The four principal, biologically matched associations were significant positive correlations between fibrotic area and the Fibroblast/ECM transcriptional score (Spearman's rho = 0.50; FDR p = 4.36×10^{-14}) and between crown-like structure density and the Macrophage/LAM transcriptional score (rho = 0.50; FDR p = 4.36×10^{-14}). A weaker, but still significant, correlation was observed between adipocyte diameter and the Adip_2 metabolic score (rho = 0.15; FDR p = 0.0438). The correlation between $CD31^+$ vascular density and the endothelial transcriptional score did not reach statistical significance after correction (rho = 0.10; FDR p = 0.148). These four associations, along with their individual-level scatter distributions colored by group, are expanded in Supplementary Figure 1C–F, which reproduces each correlation at single-sample resolution: adipocyte diameter versus Adip_2 metabolic score (Figure S1C), fibrotic area versus Fibroblast/ECM score (Figure S1D), $CD31^+$ vascular density versus endothelial score (Figure S1E), and crown-like structures versus Macrophage/LAM score (Figure S1F). Across these expanded plots, long-lived individuals were concentrated at the lower end of both axes for the fibrosis–ECM and crown-like structure–Macrophage/LAM relationships, reinforcing the attenuated fibrotic and myeloid inflammatory phenotype described above. Beyond these four matched pairs, the correlation matrix in Figure 1L also indicated additional off-diagonal associations of note, including a positive correlation between adipocyte diameter and the Macrophage/LAM score (rho =

0.43) and between adipocyte diameter and the Fibroblast/ECM score (rho = 0.29), as well as negative correlations between CD31⁺ vascular density and both the Fibroblast/ECM score (rho = -0.46) and the Macrophage/LAM score (rho = -0.39), suggesting that vascular density is inversely linked to fibrotic and lipid-associated macrophage transcriptional programs even where diameter is not directly implicated.

Differential expression analysis between the Adip_1 and Adip_2 adipocyte subtypes identified a distinct molecular signature for each state (Figure 1M): Adip_1 was characterized by higher expression of antioxidant and stress-response genes (GPX1, GPX4, SOD1, SOD2, CAT, PRDX3, PRDX6, PARP1), whereas Adip_2 showed higher expression of insulin-signaling and lipid/adipogenic metabolism genes (ADIPOQ, AKT1, AKT2, FASN, PLIN1, PDE3B, ABCA5), consistent with its insulin-responsive functional identity. The relative proportion of these two subtypes differed significantly between groups (Figure 1N), with a lower Adip_1 fraction and a higher Adip_2 fraction among long-lived individuals compared with controls.

Pseudotime reconstruction of the adipogenic differentiation trajectory (ASPC/Stem_3 → Adip_1 → Adip_2) confirmed the expected ordering of cellular states, with Stem_3 cells concentrated at low pseudotime values, Adip_1 at intermediate values, and Adip_2 at the most advanced end of the trajectory (Figure 1O). The pseudotime distribution differed significantly between groups (Kolmogorov-Smirnov test, $p = 4.16\times10^{-24}$; Figure 1P): controls showed a density peak concentrated at intermediate pseudotime values (~0.4), consistent with greater retention of cells in the Adip_1 state, whereas long-lived individuals showed a more prominent second peak at advanced pseudotime values (~0.7), indicating greater progression toward the mature Adip_2 state. This finding suggests that extreme longevity is associated with more complete adipogenic differentiation rather than a block in differentiation.

As shown in Figure 2, spatial transcriptomic profiling revealed that the senescence-associated and immunosuppressive remodeling of subcutaneous adipose tissue observed at the single-nucleus level is organized into discrete, spatially resolved niches, and that this organization is measurably reshaped in long-lived individuals. Representative spatial domain maps from a matched pair of individuals (C044, Control; L054, LLI) showed that all 13 previously defined domains — spanning adipocyte, vascular, progenitor, immune, and senescence-associated states — were present in both groups, with no domain unique to either condition (Figure 2A). Quantification across the full cohort showed that per-patient domain proportions were, on average, higher among long-lived individuals across the majority of the 13 domains, including metabolically active, vascular, and immune-related niches, as well as the Senescence_SASP domain itself (Figure 2B), indicating a more evenly redistributed spatial domain composition in LLI rather than a simple contraction of any single niche.

Despite this redistribution at the domain-classification level, direct mapping of the continuous senescence/SASP score onto tissue coordinates showed visibly fewer and less intense senescence hotspots in long-lived individuals compared with controls (Figure 2C), and both the inflammation score and the senescence score were lower among long-lived individuals at the spot level (Figure 2D). This apparent divergence — more spots categorically assigned to the Senescence_SASP domain, yet lower

senescence score intensity overall — suggests that in LLI this spatial niche is more broadly distributed but less transcriptionally active per spot, rather than absent.

Neighbor enrichment analysis around senescent spots showed that most patients in both groups exhibited D8 (imCAF-CXCL9-CXCR3^{+}Treg immunosuppressive) neighbor fractions close to the null expectation (observed/permuted ratio ≈ 1), with a subset of individuals — proportionally more frequent among LLI — reaching enrichment ratios as high as 10 (Figure 2E), indicating that strong spatial coupling between senescent and immunosuppressive niches is a patient-specific rather than a uniform group-level feature. Consistent with this, per-patient spatial cross-correlation (Spearman's rho) between the senescence score and the immunosuppressive score was numerically lower among long-lived individuals (median rho ≈ 0.13, IQR 0.04–0.24) than controls (median rho ≈ 0.19, IQR 0.12–0.26), although the two distributions overlapped substantially (Figure 2F).

Representative immunohistochemistry confirmed these spatial and transcriptomic findings at the protein level (Figure 2G): long-lived individuals showed visibly reduced CD68^{+} macrophage infiltration and p16^{+} nuclear staining, alongside markedly increased UCP1^{+} beige adipocyte staining, relative to controls. These differences were significant across every quantified metric (Figure 2H): CD68^{+} infiltrate area (adjusted p = 6.34×10^{-12}), p16^{+} senescent cell density (adjusted p = 4.06×10^{-21}), fields with p16^{+} cells (adjusted p = 1.6×10^{-21}), fields with p16^{+} adipocytes (adjusted p = 2.72×10^{-21}), p16^{+} nuclei (adjusted p = 8.3×10^{-22}), and p16 positivity score (adjusted p = 3.43×10^{-22}) were all significantly lower in long-lived individuals, whereas beige UCP1^{+} adipocyte proportion was significantly higher (adjusted p = 9.4×10^{-11}), mirroring the reduced senescent/inflammatory burden and preserved thermogenic capacity already suggested by the spatial score mapping.

Cellular neighborhood analysis showed that most of the 13 dominant-domain neighborhood categories were similarly represented between groups, with two notable exceptions: neighborhoods dominated by the ImCAF_CXCL9_CXCR3_Treg_immunosuppressive domain were markedly less frequent in LLI (~7% vs. ~11% of spot-neighborhood assignments in controls), as were Senescence_SASP-dominated neighborhoods (~7.5% vs. ~9%) (Figure 2I), while the overall number of spots per neighborhood was comparable between groups (median ≈ 55 in both) (Figure 2J), indicating that the observed differences reflect a change in niche composition rather than in neighborhood size or density. This attenuation of the immunosuppressive niche was accompanied by reduced ligand-receptor co-expression scores in long-lived individuals across all four communication axes tested — CCL2-CCR2, CXCL9-CXCR3, ITGA4-VCAM1, and TNF-TNFRSF1B (Figure 2K–N) — with the largest group separation observed for the CXCL9-CXCR3 axis that anchors the imCAF-Treg niche and for the adhesion-mediated ITGA4-VCAM1 axis, together pointing to broadly weaker pro-inflammatory intercellular signaling in the longevity phenotype.

Finally, formal spatial statistics using the Cross K-function confirmed that D8-D11 (imCAF-CXCL9-CXCR3^{+}Treg / Senescence-SASP) co-localization values clustered around or below the null expectation of complete spatial randomness in both groups, with a subset of patients in each group — including several among LLI — showing strong positive attraction values of up to ~4×10^{5} (Figure 2O). This

indicates that pronounced spatial co-localization between the senescent and immunosuppressive domains is present in a minority of individuals in both groups rather than being a categorical, group-defining feature, reinforcing the interpretation that extreme longevity is associated with an attenuated — but not fully abolished — senescence-immunosuppression spatial axis.

As shown in Figure 3, integration of a bulk transcriptomic biological-age clock, an age-adjusted molecular longevity signature, cross-omic phenotypic correlation, and chromatin accessibility profiling demonstrated that extreme longevity is associated with a measurably younger adipose molecular age and a coherent regulatory program that reinforces the cellular and spatial phenotypes described in Figures 1 and 2. A gene-expression-based elastic net/LASSO model trained to predict adipose biological age from bulk RNA-seq achieved strong performance under 10-fold cross-validation (Pearson $r = 0.86$, $R^2 = 0.74$, MAE = 5.2 years, RMSE = 6.2 years, $n = 210$; Figure 3A). Predicted adipose biological age tracked chronological age within each group, but long-lived individuals clustered below the identity line, indicating that their adipose tissue was, on average, molecularly younger than expected for their chronological age, whereas controls clustered close to or above the identity line.

To avoid conflating this finding with the trivial fact that long-lived individuals are chronologically older, we derived a residual age-acceleration metric (predicted age regressed on chronological age) and compared it between groups. Residual age acceleration was significantly lower among long-lived individuals than controls ($p < 2 \times 10^{-16}$; Figure 3B), with controls showing predominantly positive residuals and long-lived individuals predominantly negative residuals, confirming that the younger molecular age of the LLI adipose tissue is not simply an artifact of the wider chronological age range in this group. Age acceleration correlated with the principal structural and cellular phenotypes already established in Figures 1 and 2: it was inversely associated with the Adip_2 metabolic score ($r = -0.35$, FDR < 0.001) and with $CD31^+$ vascular density ($r = -0.36$, FDR < 0.001), and positively associated with adipocyte diameter ($r = 0.15$, FDR = 0.027), fibrotic area ($r = 0.34$, FDR < 0.001), and $p16^+$ senescent cell density ($r = 0.55$, FDR < 0.001) (Figure 3B). This gradient — strongest for senescence, intermediate for fibrosis and vascular density, weakest for adipocyte diameter — indicates that the biological-age clock is capturing the same fibro-inflammatory and senescence-related remodeling process identified histologically and spatially, rather than an independent or arbitrary molecular readout.

An age-adjusted LASSO model comparing long-lived individuals with controls yielded a compact longevity signature in which genes involved in mitochondrial and metabolic regulation, antioxidant defense, and adipogenic/insulin signaling (SIRT3, PRKAA1, PPARG, UCP1, SIRT1, NFE2L2, NOS3, GPX1, ADIPOQ, SOD2, FOXO3) carried positive coefficients (higher in LLI), while senescence and pro-inflammatory genes (CDKN2A, CXCL8, SERPINE1, CCL2, IL6, CDKN1A, TNF) carried negative coefficients (higher in controls) (Figure 3C). The corresponding sample-level heatmap showed consistent segregation of these two gene blocks between groups. This signature discriminated long-lived individuals from controls with an AUC of 0.90, and — critically for establishing that it is not merely a proxy for chronological age — a model combining age with the signature performed no better than age

alone (both AUC = 1.00), while the signature alone still achieved strong discrimination (AUC = 0.90) using molecular information orthogonal to the near-perfect age separation between groups (Figure 3C).

Cross-omic integration confirmed that this bulk-tissue longevity signature reproduces the phenotype identified independently by histology, single-nucleus RNA-seq, and spatial transcriptomics (Figure 3D). The longevity signature score correlated positively with the overall Healthy Adipose Aging Signature (Spearman's rho ≈ 0.6), the Adip_2 metabolic score (rho ≈ 0.45, snRNA-seq layer), and $CD31^+$ vascular density (rho ≈ 0.45, histology layer), and correlated negatively with fibrotic area and adipocyte diameter (histology layer) and, most strongly, with the spatial senescence, inflammation, and SASP composite scores (rho ≈ -0.55 to -0.6, pathway-score layer). This pattern — convergent, layer-spanning correlations in the expected direction across histological, cellular, and spatial dimensions — indicates that a single bulk-derived molecular score recapitulates the multi-layer phenotype described in Figures 1 and 2, rather than representing an isolated transcriptomic observation.

To determine whether these transcriptional differences reflect an underlying regulatory program, we profiled chromatin accessibility by scATAC-seq (Figure 3E). Differential accessibility analysis restricted to regulatory elements linked to the longevity signature genes identified a set of differentially accessible peaks and corresponding transcription-factor motifs. Motifs for PPARG, CEBPA, SREBF1, NFE2L2, KLF4, FOXO1, and NRF1 were preferentially enriched in more accessible chromatin in long-lived individuals, whereas motifs for TP53, JUN, NFKB1, STAT3, EGR1, RELA, and ATF3 were preferentially enriched in more accessible chromatin in controls. Motif accessibility (chromVAR-type z-scores) resolved by the 22 cell populations defined in Figure 1J showed that this regulatory divergence was broadly distributed across cell types but was most pronounced in myeloid populations (Macrophage_Resident, Macrophage_LAM) and dendritic cells for the pro-inflammatory motif module (EGR1, ATF3, RELA, STAT3), and in the insulin-responsive adipocyte (Adip_2) and adipogenic-committed stem populations for the metabolic/antioxidant motif module (SREBF1, NRF1), linking the regulatory signal directly to the same cell states already implicated in Figures 1 and 3D. Together, these results indicate that the longevity-associated transcriptional signature is underpinned by a distinct chromatin accessibility landscape at metabolic, adipogenic, and antioxidant regulatory elements, and by reduced accessibility at senescence- and NF-κB/AP-1-related inflammatory elements.

Figure 3F synthesizes these findings into an integrated conceptual model contrasting two adipose aging trajectories. In conventional adipose aging, adipocyte stress leads sequentially to impaired adipogenic homeostasis, senescence/SASP, expansion of a macrophage/inflammatory niche, fibroinflammatory remodeling, and ultimately vascular dysfunction. In extreme longevity, preserved adipocyte differentiation supports metabolic/thermogenic competence, attenuated senescence/SASP, reduced inflammatory intercellular communication, lower fibrosis, and preserved vascular architecture — the same sequence of phenotypes established histologically (Figure 1), spatially (Figure 2), and molecularly (Figure 3A–D) throughout the manuscript. The scATAC-derived regulatory landscape is positioned as the mechanistic layer supporting the attenuated senescence/SASP node of the longevity trajectory, linking the chromatin-level findings in Figure 3E to the multi-omic phenotype described across Figures 1–3.

As shown in Supplementary Figure 3, extended analyses confirm that the biological-age clock, the longevity molecular signature, the Healthy Aging Index, and the scATAC-seq regulatory findings summarized in Figure 3 are technically robust and reproducible, and provide the full analytical detail underlying the main figure.

The adipose biological-age clock was built following a defined analytical workflow (bulk RNA-seq input, gene filtering, supervised feature selection, elastic net/LASSO model training, cross-validation, and derivation of predicted biological age and age acceleration; Figure S3A). Predicted versus chronological age showed the same performance metrics reported in Figure 3A (Pearson r = 0.86, Spearman rho = 0.86, R^2 = 0.74, MAE = 5.2 years, RMSE = 6.2 years, n = 210), with a fitted regression line and 95% confidence interval, confirming that the correlation in the main figure reflects genuine model performance rather than a single favorable fit (Figure S3B). Repeated 10-fold cross-validation showed consistent held-out R^2 across three independent CV repeats (median R^2 approximately 0.72–0.78 per repeat), indicating that model performance was not dependent on a particular fold partition (Figure S3C). Age acceleration plotted against chronological age showed a negative slope with long-lived individuals concentrated at negative residuals across the observed age range and controls concentrated at positive residuals across their (narrower, younger) age range, without evidence of a strong residual age-dependent bias within either group (Figure S3D). A sex-adjusted linear model of age acceleration confirmed that group (LLI vs. Control) remained a significant negative predictor of age acceleration after accounting for sex, whose effect was comparatively small and did not account for the group difference (Figure S3E).

The molecular basis of the biological-age clock and of the longevity signature is detailed in Figure S3F–J. The LASSO coefficient path across the regularization path (Figure S3F) and the corresponding cross-validated error curve as a function of log(λ) (Figure S3G) show the expected monotonic increase in prediction error with increasing regularization, supporting the lambda value used for final gene selection. Ranking of all candidate genes evaluated for the longevity signature by absolute naive LASSO coefficient (Figure S3H) shows that the genes retained in the final signature (PPARG, CDKN2A, PRKAA1, NFE2L2, SERPINE1, SIRT3, UCP1, IL6, CXCL8, CCL2, ADIPOQ, GPX1, CDKN1A, SOD2, FOXO3, SIRT1, NOS3) had the largest coefficients among all genes tested, while genes such as MMP1, MMP3, CCL5, TIMP1, VCAM1, VEGFA, GDF15, HIF1A, and LEP were evaluated but not selected. The complete longevity signature heatmap across all 210 samples, ordered by group and signature score, shows a clear separation between a senescence/inflammation-high block (SERPINE1, CDKN1A, IL6, CXCL8, TNF, CCL2, CDKN2A) enriched in controls and a metabolic/antioxidant-high block (GPX1, SIRT3, FOXO3, SIRT1, ADIPOQ, SOD2, NFE2L2, UCP1, PPARG, NOS3, PRKAA1) enriched in long-lived individuals (Figure S3I), consistent with the LASSO coefficients shown in Figure 3C. Full ROC and precision-recall curves comparing an age-only model, the longevity signature alone, and a combined age-plus-signature model confirm that age alone and age-plus-signature both achieve near-perfect discrimination (AUC = 1.00, AP = 1.00), while the longevity signature alone still achieves strong discrimination using non-redundant molecular information (AUC = 0.90, AP = 0.94) (Figure S3J). The differential expression volcano plot underlying gene selection (LLI vs. Control) shows CDKN2A, VCAM1, CDKN1A, CXCL8, and CCL2 among the top genes upregulated

in controls, and ADIPOQ, SIRT3, MT-CO2, RETN, PNPLA3, and TAGLN among the top genes upregulated in long-lived individuals (Figure S3J), providing the unfiltered basis from which the final signature genes were drawn.

The Healthy Aging Index (HAI), presented here as an extended, supplementary-level composite score rather than a main-figure result, was constructed from six standardized and health-oriented components spanning three data layers: the SASP composite score and the Healthy Adipose Aging Signature (pathway-score layer), fibrotic area, $CD31^{+}$ vascular density, and adipocyte diameter (histology layer), and Adip_2 proportion (snRNA-seq layer), each contributing a defined weight to the index (Figure S3K). The HAI was significantly higher among long-lived individuals than controls (Figure S3L), consistent with a healthier composite adipose phenotype in this group. Decomposition of the index by cell-type contribution showed that the largest positive contributor to the LLI-associated HAI shift was an increased proportion of insulin-responsive Adip_2 nuclei, followed by adipogenic-committed stem, endothelial-capillary, and Macrophage_Resident populations, while the largest negative contributor was a reduced proportion of antioxidative Adip_1 nuclei (Figure S3M), mirroring the Adip_1/Adip_2 redistribution already described in Figure 1K and Figure S2A–B. The HAI correlated positively with predicted adipose biological age computed in the opposite direction expected for a healthy-aging score (i.e., lower biological age corresponded to a healthier, higher HAI among long-lived individuals; Figure S3N), providing convergent validity between the biological-age clock and the independently constructed Healthy Aging Index.

scATAC-seq quality-control metrics — fragments per nucleus, fraction of reads in peaks (FRiP), nucleosome signal ratio, and TSS enrichment — were comparable between long-lived individuals and controls (Figure S3O), indicating that the differential accessibility findings in Figure 3E are not attributable to systematic differences in library quality between groups. Single-nucleus embedding of the scATAC-seq data reproduced the same set of cell populations identified by snRNA-seq in Figure 1J, with clusters colored by cell type showing clearly separated adipocyte, stromal/progenitor, myeloid, endothelial, and lymphoid populations (Figure S3P), and the same embedding colored by group showed extensive overlap between long-lived individuals and controls within each cell-type cluster, with no group-exclusive population (Figure S3Q), paralleling the analogous snRNA-seq observation in Figure 1J that extreme longevity involves proportional rather than qualitative changes in cellular architecture.

Differential chromatin accessibility analysis restricted to curated regulatory peaks identified elements more accessible in controls (including peaks near CDKN2A, CXCL8, CCL2, VCAM1, NFKB1, JUN, and CDKN1A) and elements more accessible in long-lived individuals (including peaks near PPARG, CEBPA, ADIPOQ, PLIN1, SCD, and SELE) (Figure S3R). Transcription-factor motif enrichment across these differentially accessible peaks confirmed the directionality summarized in Figure 3E: CEBPA, KLF4, SREBF1, NFE2L2, FOXO1, PPARG, and NRF1 motifs were enriched in LLI-accessible peaks, while ATF3, RELA, EGR1, STAT3, TP53, JUN, and NFKB1 motifs were enriched in control-accessible peaks (Figure S3S). Cell-type-resolved motif activity showed that this divergence was most evident in myeloid and stromal/progenitor populations for the inflammatory motif module and in adipocyte and adipogenic-

progenitor populations for the metabolic/antioxidant motif module (Figure S3T), consistent with the cell-type pattern described for Figure 3E. Peak-to-gene regulatory link analysis connected differentially accessible enhancer and promoter elements to their putative target genes as a function of genomic distance and co-accessibility score, linking regulators such as PPARG, CEBPA, SREBF1, NFE2L2, and FOXO1 to metabolic and adipogenic target genes, and NFKB1, RELA, ATF3, TP53, EGR1, STAT3, and JUN to inflammatory and senescence-associated target genes including IL6, CCL2, CXCL10, TNF, CDKN2A, and SERPINE1 (Figure S3U). Finally, integration of chromatin accessibility with matched gene expression confirmed significant positive correlations between motif accessibility and target-gene expression for multiple regulator–gene pairs, including ATF3→SERPINE1, NFKB1→CCL3/CXCL3/IL6/TNF, TP53→CDKN2A/CDKN1A, NFE2L2→SOD2/GPX1, PPARG→ADIPOQ, FOXO1→PRKAA1/SIRT1/SIRT3, and KLF4→NOS3 (Figure S3V), providing direct molecular evidence that the chromatin accessibility changes identified in long-lived individuals are functionally coupled to the expression of the genes composing the longevity signature described in Figure 3C.

Taken together, Supplementary Figure 3 demonstrates that the reduced adipose biological age, the age-adjusted longevity molecular signature, the Healthy Aging Index, and the underlying chromatin regulatory architecture reported in Figure 3 are supported by robust cross-validated modeling, are not confounded by differences in scATAC-seq library quality, and are functionally coherent at the level of matched motif accessibility and target-gene expression — extending the histological (Figure 1) and spatial (Figure 2) characterization of extreme longevity to a validated molecular and regulatory signature of adipose tissue aging.

Discussion

Here, we present an integrated analysis combining epidemiological characterization, cytogenetic biomonitoring, oxidative stress quantification, histology, single-nucleus RNA sequencing, spatial transcriptomics, scATAC-seq, and a bulk transcriptomic biological-age clock to delineate the phenotypic, cellular, and regulatory landscape of subcutaneous adipose tissue in extreme human longevity. Our multimodal approach uncovered a coherent trajectory in which long-lived individuals (LLI) display systemically preserved genomic stability, attenuated lipid peroxidation, and an adipose tissue architecture characterized by smaller, more homogeneous adipocytes, reduced fibrosis, preserved vascularity, and a redistribution toward metabolically favorable, less senescent cellular and spatial states. This convergence across independent layers of biological organization suggests that extreme longevity is not simply the chronological extension of aging but reflects an actively maintained, distinct adipose aging trajectory.

The lower frequencies of micronuclei, nucleoplasmic bridges, and nuclear buds observed in peripheral lymphocytes and buccal cells of LLI relative to controls are consistent with a substantial body of literature linking cytogenetic damage to chronological age. Baseline micronucleus frequency in peripheral lymphocytes and buccal mucosa is well established to increase progressively across the adult lifespan (Orta and Günebakan, 2012), and, notably, the only study to have directly examined

micronucleus and chromosome nondisjunction frequencies specifically in centenarians reported that these individuals do not show the expected age-related accumulation of chromosomal damage seen in younger elderly cohorts (Wojda et al., 2007), a pattern our data reproduce and extend to buccal degenerative parameters (condensed chromatin, karyorrhexis, karyolysis, pyknosis). Because buccal micronuclei have been proposed as a cumulative, non-invasive biomarker of biological rather than merely chronological aging (Bolognesi and Fenech, 2019), the markedly lower buccal and lymphocyte damage indices in LLI support the interpretation that survival to extreme old age is associated with preserved genomic maintenance capacity rather than simple selection against individuals who happened not to accumulate damage. The unchanged Nuclear Division Index further indicates that this reduced damage burden is not attributable to differences in lymphocyte proliferative kinetics, reinforcing a genuine difference in genome integrity rather than a technical or cell-cycle artifact.

The lower plasma malondialdehyde (MDA) concentration in LLI parallels this genomic stability. MDA is the most widely used circulating biomarker of lipid peroxidation, and its levels have repeatedly been reported to rise with advancing chronological age across tissues and biofluids, particularly in postmitotic, lipid-rich tissues (Tsikas et al., 2023). Adipose tissue, by virtue of its high polyunsaturated fatty acid content, is intrinsically vulnerable to this process, and the coupling we observe between lower MDA and better-preserved cytogenetic indices is consistent with the broader hypothesis that reduced systemic oxidative burden in LLI limits both lipid and nuclear damage accumulation, echoing prior findings that centenarians maintain more effective redox and mitochondrial defenses than septuagenarian or younger elderly comparators (Passarino et al., 2016).

Regarding lifestyle correlates, the higher prevalence of widowhood and lower prevalence of alcohol consumption and reported physical activity among LLI are best interpreted in light of the specific demographic and functional profile of this population rather than as evidence of a protective effect of inactivity. Widowhood is a near-mechanical consequence of surviving one's cohort into the tenth and eleventh decades of life, while systematic reviews specifically focused on centenarians report that this group is consistently frailer and less physically active than younger-old comparators, with low physical activity being among the most prevalent frailty criteria identified (Freitas et al., 2022 [Fragilidade e atividade física em centenários]). This pattern is best understood through reverse causation and survivor selection rather than a causal benefit of inactivity: individuals who reach 100 years of age typically do so with reduced functional reserve, which limits activity participation, even as their underlying molecular and cellular aging trajectory - as captured by our cytogenetic, oxidative stress, and multi-omic adipose data - remains comparatively favorable. Similarly, alcohol intake has been associated with lower circulating levels of the anti-aging hormone Klotho (Fromm et al., 2023), and the lower alcohol consumption among LLI may plausibly contribute to, rather than merely correlate with, the higher Klotho levels and more favorable biomarker profile we observed in this group.

At the tissue level, the histological remodeling profile identified in LLI - smaller, more homogeneous adipocytes, a shift toward small-adipocyte hyperplasia rather than hypertrophy, reduced pericellular and septal fibrosis, and increased CD31 + microvascular density - recapitulates, in an inverted direction, the

canonical signature of unhealthy adipose tissue expansion described in obesity and conventional aging. Adipocyte hypertrophy, rather than hyperplasia, is a well-established driver of adipose tissue dysfunction, because it exceeds the tissue's vascular and matrix remodeling capacity, precipitating local hypoxia, fibrosis, and macrophage recruitment around dying adipocytes in the form of crown-like structures (CLS), a histological hallmark of adipose inflammation and insulin resistance (cf. reviews on adipose tissue macrophages and CLS biology). Aging itself is associated with an increase in the proportion of pro-inflammatory (M1-like) adipose tissue macrophages even when total macrophage content is unchanged (Jia et al., 2021 [J Physiol Sci]), and our finding of reduced CD68 + infiltration, fewer macrophage/lipid-associated (LAM) cells at the single-nucleus level, and lower crown-like structure density in LLI is consistent with an attenuation of this canonical inflammaging process rather than its absence. The preserved-to-expanded microvascular architecture we observed similarly diverges from the vascular rarefaction typically reported in aged and fibrotic adipose depots, suggesting that the LLI phenotype specifically resists the fibro-vascular uncoupling that characterizes conventional adipose aging.

The single-nucleus transcriptomic data provide a cellular explanation for this histological divergence. The relative expansion of the insulin-responsive Adip_2 subtype and contraction of the antioxidative Adip_1 subtype among LLI directly parallels findings from single-nucleus profiling of human subcutaneous white adipose tissue across the adult lifespan, in which Adip_1 (anti-oxidative) and vascular/pre-adipocyte populations - but not Adip_2 (insulin-responsive) - showed senescence-associated (SenMayo) transcriptional enrichment and elevated p16 positivity with older age (Whytock et al., 2024). Our observation that the Adip_1-to-Adip_2 balance is shifted toward the non-senescent, metabolically active Adip_2 state in LLI, together with concordant reductions in senescent p16 + nuclei and CD68 + macrophages by immunohistochemistry, indicates that this cell-state redistribution is not merely a transcriptomic curiosity but corresponds to a measurably lower senescent burden at the protein level. The accompanying pseudotime findings - greater progression toward the mature Adip_2 endpoint of the adipogenic trajectory in LLI - further suggest that this redistribution reflects more complete, rather than blocked, adipogenic differentiation, consistent with reports that impaired adipogenic differentiation and progenitor senescence, rather than differentiation per se, underlie age- and obesity-related adipose dysfunction (Xu et al., 2024 [M2 macrophage-derived TGF-β and progenitor senescence]).

At the level of intercellular signaling, the attenuated senescence-associated secretory phenotype (SASP) transcriptional and spatial signature in LLI is mechanistically consistent with the established role of NF-κB, in cooperation with C/EBPβ, as the master transcriptional regulator of SASP factor expression, including IL-6, IL-8, and other pro-inflammatory mediators (Chien et al., 2011). The lower TNF-α, TGF-β1, and MPO levels, reduced ligand-receptor co-expression across the CCL2-CCR2, CXCL9-CXCR3, ITGA4-VCAM1, and TNF-TNFRSF1B axes, and the less frequent imCAF-CXCL9-CXCR3 + Treg immunosuppressive and Senescence_SASP-dominated cellular neighborhoods observed spatially in LLI together point to a systemic dampening of this NF-κB-anchored inflammatory circuit, rather than the wholesale absence of senescent cells - a distinction reinforced by our finding that Senescence_SASP domain proportions were not simply reduced, but redistributed with lower per-spot transcriptional

intensity, in LLI. This pattern is compatible with the broader concept that healthy extreme longevity involves the containment rather than the elimination of senescence, a distinction increasingly emphasized in the cellular senescence literature.

The pronounced sex differences we identified in several adipokines and inflammatory biomarkers are also consistent with, and extend, the existing literature on sexual dimorphism in adipose endocrine function during aging. Higher adiponectin in women relative to men in both study groups mirrors the well-documented 1.5- to 2-fold higher circulating adiponectin in women across the lifespan (Pajvani et al., 2003, as reviewed), and the specifically elevated adiponectin observed among centenarians and their offspring - independent of BMI and sex - has previously been proposed as a heritable, longevity-associated trait (Atzmon et al., 2008). Similarly, the higher leptin levels in women than men in both groups reproduce a consistent sex difference attributed to greater subcutaneous fat mass and estrogen-mediated leptin gene expression, while the sex difference in GDF-15 favoring men specifically among controls, but not among LLI, is noteworthy: GDF-15 is an established stress-responsive, mitochondrially linked biomarker whose levels rise with age, frailty, and multimorbidity (Tian et al., 2025), and its convergence between sexes among LLI may indicate a more uniform, lower-stress phenotype in this group independent of the sex-specific patterns seen in typical aging. The lower Klotho levels in control men relative to control women, and the overall difference in Klotho between LLI and controls, align with Klotho's established role as an anti-aging hormone with antioxidant, insulin-sensitizing, and lifespan-modulating properties in animal models (Kurosu et al., 2005), and with human data linking lower Klotho to frailty, worse cognition, and higher mortality risk (Ellam and Fotheringham, 2024).

The bulk transcriptomic and chromatin accessibility findings provide a unifying, mechanistically grounded explanation for these convergent phenotypes. The gene-expression-based biological-age clock's strong cross-validated performance, and, critically, the persistence of significantly lower residual age acceleration in LLI even after regressing out chronological age, addresses the central confound in any longevity biomarker study: whether molecular differences between LLI and controls reflect a genuine biological phenotype or simply track the wider age range of the LLI group. The correlation structure linking age acceleration to senescent cell density, fibrotic area, and vascular density recapitulates, at the transcriptomic level, the same fibro-inflammatory-senescence axis identified histologically and spatially. The longevity signature itself - with SIRT3, PRKAA1 (AMPK), PPARG, UCP1, SIRT1, NFE2L2 (NRF2), NOS3, GPX1, ADIPOQ, SOD2, and FOXO3 elevated in LLI - assembles several of the most robust human longevity-associated genes identified in prior genetic association studies into a single coherent transcriptional program. FOXO3 in particular is among the most consistently replicated human longevity genes across multiple independent centenarian cohorts spanning several ethnicities (Willcox et al., 2008), and its co-elevation here alongside SIRT1 - its principal upstream deacetylase regulator in the nutrient-sensing IIS/AMPK-SIRT-FOXO axis - together with the antioxidant genes GPX1, SOD2, and NFE2L2, suggests that the longevity signature we identified in adipose tissue is not an isolated depot-specific observation but a tissue-level readout of systemic longevity-associated regulatory programs previously described primarily at the genetic or peripheral blood level. Conversely, the negative-coefficient, control-enriched genes (CDKN2A, CXCL8, SERPINE1, CCL2, IL6, CDKN1A, TNF) constitute a

canonical senescence/SASP gene set, again converging with the NF-κB-driven SASP biology discussed above. The reduced adipose UCP1 expression and beige-adipocyte proportion typically reported with human aging (Zoico et al., 2019) is inverted in our LLI cohort, whose elevated UCP1 within the longevity signature and increased UCP1 + beige adipocyte staining suggest a preserved thermogenic and metabolically flexible adipocyte phenotype uncommon in conventional aging.

Finally, the chromatin accessibility landscape offers a plausible upstream regulatory basis for this transcriptional divergence. The preferential accessibility of PPARG, CEBPA, SREBF1, NFE2L2, KLF4, FOXO1, and NRF1 motifs in LLI, contrasted with preferential accessibility of TP53, JUN, NFKB1, STAT3, EGR1, RELA, and ATF3 motifs in controls, mirrors the transcription factor circuitry established in the broader adipogenesis and senescence literature: PPARG and CEBPA are the master transcriptional regulators of adipocyte differentiation and are similarly implicated in macrophage anti-inflammatory (M2) polarization (Jiang et al., 2023 [adipose tissue macrophages as therapeutic targets]), while RelA/p65-containing NF-κB, together with AP-1 family members such as JUN, constitutes the master transcriptional driver of the SASP (Chien et al., 2011). That this regulatory divergence localizes predominantly to myeloid and adipogenic-progenitor populations in our cell-type-resolved motif analysis lends further, cell-type-specific support to the concept that the LLI adipose phenotype reflects coordinated, lineage-specific epigenetic reprogramming rather than a uniform, tissue-wide shift.

Several limitations of our study warrant consideration. First, although the overall sample size (n = 210) is substantial for a deeply phenotyped centenarian/nonagenarian cohort, the number of individuals contributing to each single-cell, spatial, and chromatin accessibility layer is necessarily smaller, which may limit statistical power to detect subtle, especially rare, cell-population or niche-level differences; associated descriptive analyses, such as the per-cell-type composition patterns in Supplementary Fig. 2, should accordingly be interpreted as complementary and directional rather than independently powered comparisons. Second, the cross-sectional design precludes definitive causal inference: whether the preserved genomic stability, attenuated senescence, and favorable adipose regulatory landscape we describe are a cause or a consequence of extreme longevity - or both, in a self-reinforcing loop - cannot be resolved without longitudinal or interventional data. Third, while the convergence of independent modalities (cytogenetics, histology, snRNA-seq, spatial transcriptomics, bulk RNA-seq, and scATAC-seq) toward the same fibro-inflammatory-senescence axis provides strong internal, cross-platform validation, functional perturbation studies - for example, targeted modulation of the PPARG/CEBPA or NF-κB/AP-1 regulatory modules in adipose progenitor or macrophage populations - will be required to move from the correlative, multi-omic atlas presented here toward mechanistic and, ultimately, therapeutic conclusions. Finally, as with most extreme-longevity cohorts, survivorship bias is an inherent feature of the study design: individuals who reached the LLI threshold necessarily represent survivors of a selection process operating across their entire lifespan, and the extent to which the phenotype described here is present earlier in life, and therefore potentially modifiable, remains an open question for future prospective research.

Taken together, our findings indicate that extreme human longevity is associated with a coordinated, multi-layered adipose tissue phenotype - spanning genomic stability, oxidative stress, tissue architecture, single-cell composition, spatial niche organization, and chromatin regulatory state - that collectively favors preserved adipogenic differentiation, attenuated senescence and inflammatory signaling, and maintained vascular and thermogenic competence. This integrated atlas provides a prioritized set of candidate targets, from FOXO3-SIRT1-AMPK metabolic regulators to the NF-κB/AP-1-driven SASP and CXCR3-anchored immunosuppressive niche, for future mechanistic studies aimed at understanding, and potentially recapitulating, the adipose aging trajectory associated with exceptional human longevity.

Materials and Methods

Study design and participants

This was an observational, analytical, cross-sectional study comparing long-lived individuals (LLI) and controls, integrating sociodemographic, clinical, biochemical, cytogenetic, and multi-omics data (single-nucleus transcriptomics, spatial transcriptomics, bulk transcriptomics, and chromatin accessibility) from subcutaneous adipose tissue. The sample comprised 210 unrelated participants: 140 LLIs (age ≥85 years) and 70 controls (70–75 years), an age range close to the average life expectancy of the Brazilian older population. This approach was based on the rationale that older adults whose age is close to the population life expectancy are more strongly influenced by environmental than genetic factors, whereas individuals who substantially exceed population life expectancy tend to be enriched for protective genetic and biological factors (Willcox et al., 2008; Anselmi et al., 2009; Flachsbart et al., 2009).

Participants were recruited from Belo Horizonte and Nova Lima, Minas Gerais, Brazil, and clinically evaluated by a team of geriatricians. The groups were sex-matched. The study was approved by the institutional Research Ethics Committee and conducted in accordance with the Declaration of Helsinki and the World Medical Association Code of Ethics. Written informed consent was obtained from all participants or their legally authorized representatives/caregivers.

A face-to-face interview was conducted by trained researchers using a structured questionnaire adapted from the International Commission for Protection against Environmental Mutagens and Carcinogens (Carrano and Natarajan, 1988), complemented by items assessing functional capacity and quality of life adapted from the Medical Outcomes Study 36-Item Short-Form Health Survey (SF-36) for the Brazilian population (Ware and Sherbourne, 1992). The questionnaire assessed sociodemographic and socioeconomic characteristics (age, sex, race/skin color, marital status, educational attainment, monthly income, and housing type), lifestyle variables (smoking, alcohol consumption, physical activity, and frequency of vegetable and fruit consumption), and medical history (hypertension, diabetes mellitus, neurodegenerative disease, neoplasia, and respiratory disease), confirmed through medical records and review of current medications.

To minimize confounding factors in the cytogenetic and oxidative stress analyses, participants selected for these sub-analyses were required to be nonsmokers, non-alcohol consumers, non-users of

antioxidant supplements, and free from diagnostic radiographic exposure or recent surgical procedures (<6 months).

Anthropometric, clinical, and biochemical assessment

Weight and height were measured using a calibrated stadiometer and scale (Filizola, São Paulo, Brazil), and body mass index (BMI) was calculated and classified according to Pan American Health Organization criteria. Waist and hip circumferences were measured using a non-stretch anthropometric tape (Sanny, São Paulo, Brazil), and the waist-to-hip ratio (WHR) was classified according to World Health Organization cutoff points (<1.0 for men; <0.85 for women). Subscapular skinfold thickness and body fat percentage were obtained by bioelectrical impedance analysis using an InBody device.

Systolic and diastolic blood pressure were measured with participants in a seated position after a period of rest using a calibrated aneroid sphygmomanometer (Welch Allyn or equivalent). Fasting venous blood (8–10 mL) was collected into tubes containing 5% EDTA (Vacuette, Greiner Bio-One, Austria) for hematological, cytogenetic, and molecular analyses, and into serum tubes for biochemical and ELISA-based biomarker analyses.

Complete blood counts (hemoglobin, hematocrit, leukocytes, neutrophils, lymphocytes, and platelets) and standard clinical biochemistry parameters (fasting glucose, glycated hemoglobin [HbA1c], insulin, HOMA-IR, total cholesterol, LDL-C, HDL-C, triglycerides, AST, ALT, creatinine, urea, albumin, high-sensitivity C-reactive protein, ferritin, fibrinogen, NT-proBNP, high-sensitivity troponin I, vitamin D, vitamin B12, folate, and homocysteine) were determined in a certified clinical laboratory using an automated analyzer (Cobas 411/601, Roche Diagnostics) and standardized enzymatic, immunoturbidimetric, and chemiluminescence methods.

Circulating inflammatory, metabolic, cardiovascular, and aging-related biomarkers—including IL-6, TNF-α, IL-1β, MCP-1/CCL2, TGF-β1, GDF-15, PAI-1/SERPINE1, Klotho, FGF-21, IGF-1, adiponectin, leptin, neurofilament light chain (NfL), and myeloperoxidase (MPO)—were quantified in plasma/serum by enzyme-linked immunosorbent assay (ELISA), in duplicate, with optical density readings obtained using a microplate reader (SpectraMax iD3, Molecular Devices, USA).

IL-6 Quantikine HS ELISA (R&D Systems, cat. HS600C), TNF-α Quantikine HS ELISA (R&D Systems, cat. HSTA00E), IL-1β Quantikine HS ELISA (R&D Systems, cat. HSLB00D), Human CCL2/MCP-1 DuoSet ELISA (R&D Systems, cat. DY279), Human TGF-β1 DuoSet ELISA (R&D Systems, cat. DY240), Human GDF-15 Quantikine ELISA (R&D Systems, cat. DGD150), Human Serpin E1/PAI-1 Quantikine ELISA (R&D Systems, cat. DSE100), Human/Mouse Klotho DuoSet ELISA (R&D Systems, cat. DY5334), Human FGF-21 Quantikine ELISA (R&D Systems, cat. DF2100), Human IGF-I Quantikine ELISA (R&D Systems, cat. DG100), Human Adiponectin/Acrp30 Quantikine ELISA (R&D Systems, cat. DRP300), Human Leptin Quantikine ELISA (R&D Systems, cat. DLP00), Human NF-L ELISA (Uman Diagnostics/Quanterix Simoa, according to the required sensitivity), and Human Myeloperoxidase DuoSet ELISA (R&D Systems, cat. DY3174) were used.

Genomic DNA was extracted from peripheral blood leukocytes using a standard salting-out protocol (Miller et al., 1988), with concentration and purity (A260/A280) assessed using a NanoDrop 2000 spectrophotometer (Thermo Fisher Scientific, Wilmington, DE, USA).

Assessment of cytogenetic damage

Cytokinesis-block micronucleus assay (CBMNcyt)

Genomic damage in peripheral blood lymphocytes was assessed using the CBMNcyt assay according to the method of Fenech and Morley (1985), with scoring criteria updated by Bolognesi and Fenech (2013). Whole-blood lymphocyte cultures were established in duplicate, stimulated with phytohemagglutinin (PHA-M, Gibco/Thermo Fisher Scientific or Sigma-Aldrich), and cytokinesis was blocked with cytochalasin-B (Sigma-Aldrich, cat. C6762) to generate binucleated cells.

For each participant, 2,000 binucleated cells with well-preserved cytoplasm (1,000 cells per duplicate culture) were evaluated by optical microscopy at 1000× magnification for the frequency of micronuclei (MN), nucleoplasmic bridges (NPB), and nuclear buds (NBUD), expressed per 1,000 binucleated cells. The Nuclear Division Index (NDI), reflecting the proliferative and cell-cycle status of the culture, was calculated from 1,000 cells per individual according to Eastmond and Tucker (1989).

Buccal micronucleus cytome assay (BMNcyt)

Exfoliated buccal epithelial cells were collected from both cheeks using a pre-moistened cytological brush (cytobrush) after rinsing the mouth with water. Cells were resuspended in chilled 0.9% saline solution and repeatedly centrifuged and washed. Cell suspensions were smeared onto slides, air-dried, fixed in 80% methanol, and stained with Leishman stain.

Slides were blindly evaluated by a single trained observer using microscopy at 1000× magnification according to the criteria of Thomas et al. (2009), which capture biomarkers of DNA damage (MN, NBUD), cell death (condensed chromatin, karyorrhexis, karyolysis, and pyknosis), and cytokinetic/proliferative status (binucleated cells). A total of 2,000 cells were evaluated per individual (1,000 per duplicate slide), with results expressed per 1,000 cells.

Oxidative stress: plasma malondialdehyde (MDA)

Lipid peroxidation was assessed by quantifying plasma malondialdehyde (MDA) as a thiobarbituric acid-reactive substance using a method adapted from Buege and Aust (1978). Plasma was mixed with an acidic thiobarbituric acid (TBA) reagent containing butylated hydroxytoluene (BHT) to prevent ex vivo MDA generation, heated at 95°C, cooled, and centrifuged. The MDA-TBA chromogen was quantified by high-performance liquid chromatography with diode-array detection (HPLC-DAD; Agilent 1260 Infinity II, Agilent Technologies, USA; C18 column), in duplicate, following the method of Antunes et al. (2008). Results were expressed as μmol/L of plasma.

Histology and immunohistochemistry of subcutaneous adipose tissue

Subcutaneous adipose tissue biopsies were fixed in 10% neutral buffered formalin, dehydrated through a graded ethanol series, cleared, and paraffin-embedded. Sections of 5 µm were obtained using a rotary microtome (Leica RM2245).

Hematoxylin and eosin (H&E) staining was used for general morphology and adipocyte size assessment; Masson's trichrome staining was used to visualize and quantify collagen/fibrosis deposition; and immunohistochemistry for CD31 (PECAM-1) was used to identify vascular endothelium, following a standard indirect immunoperoxidase protocol with antigen retrieval, endogenous peroxidase blocking, incubation with the primary antibody (anti-CD31 clone JC70A, Dako/Agilent), and detection using a horseradish peroxidase (HRP)-conjugated secondary antibody and diaminobenzidine (DAB) chromogen, with hematoxylin counterstaining.

Immunohistochemistry was similarly performed for CD68 (pan-macrophage marker; clone PG-M1, Dako/Agilent), p16^INK4a (cellular senescence marker; clone E6H4, CINtec Histology kit, Roche), and UCP1 (beige/thermogenic adipocyte marker; anti-UCP1 antibody, Abcam ab10983) on serial sections.

Digitized images (Zeiss Axio Scan.Z1) were analyzed using the open-source ImageJ/Fiji software (Schneider et al., 2012; dos Santos et al., 2024), supplemented when necessary by QuPath (Bankhead et al., 2017; dos Santos et., 2024) for automated and semi-automated morphometric quantification.

From H&E sections, adipocyte diameter was measured in individually segmented adipocytes per field, and the following parameters were derived for each individual: mean adipocyte diameter, coefficient of variation (CV) of adipocyte diameter (an index of adipocyte size heterogeneity), and the proportion of small adipocytes (<50 µm) and large adipocytes (>100 µm). These parameters were used to distinguish a hyperplastic remodeling pattern (small adipocytes) from a hypertrophic pattern (large adipocytes). In Masson's trichrome sections, the fibrotic area fraction (collagen-positive area), a semiquantitative collagen density score (0–3), and fibrous septa thickness were quantified. In CD31-stained sections, microvascular density was expressed as CD31+ vessels per mm².

Crown-like structures (CLS), defined as clusters of CD68+ macrophages surrounding a necrotic or dying adipocyte, were counted per standardized field area according to established histological criteria for this marker of adipose tissue inflammation (Zoico et al., 2019).

The burden of p16+ senescent cells was quantified as p16+ nuclear density, percentage of p16+ fields, percentage of fields containing p16+ adipocytes, percentage of p16+ nuclei, and a composite p16 positivity score. UCP1+ beige adipocyte content was expressed as the percentage of UCP1+ area. Between-group comparisons for all histomorphometric parameters were adjusted for multiple comparisons (see Statistical Analysis).

Single-nucleus RNA sequencing (snRNA-seq)

Nuclei were isolated from subcutaneous adipose tissue frozen in liquid nitrogen using a mechanical/detergent-based protocol optimized for lipid-rich tissue (e.g., NP-40/Nonidet-based lysis buffer followed by filtration and gradient purification). Single-nucleus transcriptome libraries were prepared using a droplet-based platform (10x Genomics Chromium Next GEM Single Cell 3' Reagent Kit v3.1, 10x Genomics, Pleasanton, CA, USA), followed by sequencing on an Illumina NovaSeq X Plus platform (Illumina Inc., San Diego, CA, USA) using paired-end sequencing.

Raw reads were demultiplexed and aligned to the human reference genome (GRCh38), and gene-barcode count matrices were generated using the Cell Ranger pipeline (10x Genomics). Downstream processing was performed in R using Seurat (Hao et al., 2024).

Nuclei were filtered according to the number of detected genes and the fraction of mitochondrial gene expression to exclude low-quality nuclei and doublets. Gene expression was normalized using log-normalization and scaled, with regression of the mitochondrial fraction and total UMI count as potential confounding covariates.

Highly variable genes were identified (FindVariableFeatures), principal component analysis (PCA) was performed, and the effective number of principal components was selected based on the inflection point of the explained variance plot (elbow plot). Harmony (Korsunsky et al., 2019) was applied to integrate samples across individuals and correct for batch effects. Nuclei were clustered using a graph-based shared-nearest-neighbor approach across a range of resolutions and visualized using Uniform Manifold Approximation and Projection (UMAP).

Clusters were annotated using canonical marker genes and literature-derived markers into 22 cell types and subtypes encompassing adipocyte compartments (Adip_1 antioxidant, Adip_2 insulin-responsive), stromal/progenitor compartments (Stem_1_stemlike, Stem_2_Aregs, Stem_3_adipogenic_committed, Stem_4_fibroinflammatory, fibroblast, pericyte/smooth muscle cell), endothelial compartments (arterial, venous, capillary, lymphatic, activated), myeloid compartments (resident macrophage, LAM macrophage [lipid-associated macrophage], dendritic cell, monocyte, mast cell), and lymphoid compartments (B cells, CD4 T cells, CD8 T cells, regulatory T cells, and NK cells).

Cellular composition was quantified for each individual as the percentage of nuclei assigned to each cell type. Differential expression between the Adip_1 and Adip_2 subtypes was assessed using the Wilcoxon test (Seurat's FindMarkers function), requiring expression in >10% of nuclei in at least one group and an average fold change >1.5, with Bonferroni correction. Module/pathway scores for the Adip_2 metabolic, Fibroblast/ECM, Endothelial, and Macrophage/LAM transcriptional programs were calculated per individual by aggregating the expression of curated sets of marker/effector genes for each program using an approach analogous to Seurat's AddModuleScore. These scores were used for cross-correlation with the corresponding histological parameters.

Adipogenic differentiation trajectory analysis (pseudotime)

The adipogenic differentiation trajectory of stem/progenitor cells (Stem_3_adipogenic_committed), progressing through the Adip_1 antioxidant state to the Adip_2 insulin-responsive state, was reconstructed using Monocle3 (Cao et al., 2019).

A principal graph was learned over the batch-corrected, dimensionally reduced dataset (learn_graph, with automatic partitioning and loop-closing parameter), cells were ordered in pseudotime with root nodes anchored in the Stem_3 population (order_cells), and pseudotime distributions by individual and study group were compared using the two-sample Kolmogorov-Smirnov test.

Histology-transcriptomics integration

Per-individual Spearman correlations were calculated between four histological metrics (adipocyte diameter, fibrotic area, CD31+ vascular density, and crown-like structure density) and the four corresponding snRNA-seq module scores (Adip_2 metabolic, Fibroblast/ECM, Endothelial, and Macrophage/LAM), with false discovery rate (FDR) correction applied to the correlation matrix.

Spatial transcriptomics

The spatial gene expression profile of subcutaneous adipose tissue was obtained using a spot-based spatial platform (10x Genomics Visium Spatial Gene Expression, 55-µm-diameter spots, 100-µm center-to-center spacing), following the manufacturer's tissue optimization, permeabilization, reverse transcription, and library preparation protocols, with sequencing performed on an Illumina platform. Reads were aligned to the human reference genome, and spot-level expression matrices were generated using the Space Ranger pipeline (10x Genomics). Spots overlapping tissue and meeting minimum read-count and gene-detection thresholds were retained. Downstream analysis was performed using Seurat following a standard spatial workflow: normalization using SCTransform, regression of the mitochondrial fraction and total UMI count as covariates, PCA based on highly variable genes, and unsupervised spatial clustering across a range of resolutions to identify canonical spatial domains.

Thirteen recurrent spatial domains were defined across the cohort, encompassing adipocyte states (classical metabolic, angiogenic), progenitor states (perivascular ASPC), vascular/endothelial states, immune states (lymphoid immune surveillance, macrophage-LAM/CLS, mast cell), fibrotic/extracellular matrix states, thermogenic states (beiging), and senescence-associated states (Senescence_SASP, immunosuppressive imCAF-CXCL9-CXCR3+Treg [D8 domain]), in addition to a high mitochondrial/ribosomal metabolic domain.

Domain proportions per patient were expressed as the fraction of spots assigned to each domain.

Deconvolution of cell types within spatial spots, mapping the 22 cell types defined by snRNA-seq onto spatial coordinates, was performed using Cell2location (Kleshchevnikov et al., 2022), using the paired snRNA-seq dataset as a reference for a negative binomial regression model. Reference gene filtering and mapping were performed according to the software's recommended workflow, including minimum

cell/expression thresholds for reference genes, estimated number of cells per spot, detection sensitivity, and training-epoch hyperparameters.

Composite pathway scores for senescence, inflammation, and the senescence-associated secretory phenotype (SASP) were calculated for each spot from curated senescence/SASP and inflammatory gene sets and mapped onto tissue coordinates to visualize senescence "hotspots." Neighbor enrichment analysis around senescent spots (D8 domain, immunosuppressive imCAF-CXCL9-CXCR3+Treg, relative to the Senescence_SASP domain) was performed by comparing the observed fraction of D8 neighbors with a null distribution generated by spatial permutation, expressed as an observed/permuted ratio (ratio = 1 indicating no enrichment).

Patient-level spatial cross-correlation between the senescence score and the immunosuppressive pathway score was calculated using Spearman correlation across spatial coordinates. Cellular neighborhood analysis was performed by assigning each spot to a neighborhood defined by its k nearest spatial neighbors and classifying neighborhoods according to the predominant domain, following standard spatial neighborhood enrichment approaches for spot-resolution spatial transcriptomics (conceptually analogous to squidpy-type neighborhood enrichment; Palla et al., 2022).

Ligand-receptor coexpression analysis

Ligand-receptor coexpression scores per spot were calculated for four candidate communication axes anchoring the senescence/immunosuppressive niche—CCL2-CCR2, CXCL9-CXCR3, ITGA4-VCAM1, and TNF-TNFRSF1B—using a ligand × receptor coexpression scoring approach conceptually consistent with established cell-cell communication inference frameworks (e.g., CellChat; Jin et al., 2021), applied at spot resolution.

Formal spatial statistics: cross-K function

Spatial colocalization between domains D8 (immunosuppressive imCAF-CXCL9-CXCR3+Treg) and D11 (Senescence-SASP) was formally tested using the bivariate cross-K function (Ripley's K), implemented in the R package spatstat (Baddeley and Turner, 2005; Baddeley et al., 2015), by comparing the observed K function with the theoretical expectation under complete spatial randomness (Poisson process). The mean difference between the observed and theoretical K functions was used as a patient-level attraction/repulsion statistic, with positive values indicating spatial attraction (colocalization) and values close to zero indicating spatial randomness.

Bulk RNA sequencing, adipose biological age clock, and molecular longevity signature

Bulk RNA sequencing was performed on subcutaneous adipose tissue from all 210 participants using either total RNA or polyadenylated mRNA libraries (e.g., Illumina TruSeq Stranded mRNA kit), sequenced on a NovaSeq 6000/Illumina NovaSeq X Plus platform. Raw reads were quality-filtered and aligned to the human reference genome (e.g., using STAR), and gene-level count/normalized expression values were

generated using a standard bulk RNA-seq quantification pipeline (salmon/featureCounts followed by DESeq2/edgeR normalization).

Adipose biological age clock

A gene expression-based biological age predictor was constructed according to a predefined analytical workflow (Figure S3A): (1) filtering of input adipose bulk RNA-seq data; (2) gene filtering, removing genes with low or non-variable expression; (3) supervised feature selection based on correlation with chronological age; (4) model training using regularized elastic net/LASSO regression implemented in the R package glmnet (Friedman et al., 2010), with chronological age as the outcome; (5) model evaluation using 10-fold cross-validation repeated across three independent partitions to assess robustness; and (6) derivation for each sample of the predicted adipose biological age and corresponding residual age acceleration (predicted age minus chronological age), additionally regressed on chronological age to remove the mechanical dependence between predicted age and the actual age range of the cohort.

Model performance was summarized using Pearson and Spearman correlation coefficients, coefficient of determination (R^2), mean absolute error (MAE), and root mean square error (RMSE). A sex-adjusted linear model of age acceleration was fitted to confirm that the group effect (LLI vs. Control) was independent of sex.

Age-adjusted molecular longevity signature

An independent age-adjusted LASSO logistic regression model (glmnet; Friedman et al., 2010) was trained to discriminate LLIs from controls based on bulk adipose gene expression, including chronological age as a covariate to isolate signature genes carrying information beyond age.

The regularization parameter (λ) was selected by minimizing cross-validated deviance, and the coefficient path was examined across the full regularization range.

Candidate genes were ranked according to the magnitude of their naive absolute LASSO coefficients, and the final signature retained genes with the largest non-zero coefficients at the selected λ. Model discriminative performance was evaluated using the area under the ROC curve (AUC) and average precision (area under the precision-recall curve), comparing an age-only model, the isolated longevity signature, and a combined age + signature model to formally test whether the signature carried information orthogonal to chronological age. Differential expression between LLIs and controls underlying signature gene selection was assessed using the Wilcoxon test with FDR correction and visualized as a volcano plot (log2 fold-change vs. −log10[FDR]).

Cross-correlation of the longevity signature

The individual longevity signature score was correlated (Spearman rho, FDR-corrected) with independent phenotypic layers, including histological parameters (adipocyte diameter, fibrotic area, CD31+ vascular density), snRNA-seq module scores (Adip_2 metabolic, Fibroblast/ECM, Macrophage/LAM), and spatial

pathway scores (senescence, inflammation, composite SASP, and an overall Healthy Adipose Aging Signature).

Healthy Aging Index (HAI)

A composite Healthy Aging Index score was constructed from six standardized, health-oriented components encompassing three data layers: the composite SASP score and Healthy Adipose Aging Signature (pathway-score layer); fibrotic area, CD31+ vascular density, and adipocyte diameter (histological layer); and the proportion of Adip_2 cells (snRNA-seq layer). Each component was standardized (z-score) and combined into a weighted composite score (weights presented in Figure S3K), oriented such that higher values indicated a healthier adipose phenotype. HAI was compared between groups, decomposed by cell-type contribution (delta in cell proportion, LLI minus Control, across the 22 annotated populations), and correlated with predicted adipose biological age to provide convergent validation with the biological age clock.

Single-nucleus chromatin accessibility sequencing (scATAC-seq)

Chromatin accessibility was profiled in nuclei isolated from the same subcutaneous adipose tissue samples using a droplet-based single-nucleus ATAC-seq platform (10x Genomics Chromium Next GEM Single Cell ATAC Reagent Kit v2), with sequencing on an Illumina NovaSeq 6000/Illumina NovaSeq X Plus platform. Raw data were processed using the Cell Ranger ATAC pipeline (10x Genomics), aligned to the human reference genome, and downstream analysis was performed in R using Signac (Stuart et al., 2021).

A common peak set was generated by merging peaks across samples, and a consensus feature-by-nucleus matrix was quantified. Quality control was performed based on fragments per nucleus, fraction of reads in peaks (FRiP), nucleosome signal ratio, and transcription start site (TSS) enrichment score, with low-quality nuclei excluded using threshold-based filtering. These QC metrics were compared between groups to exclude systematic library-quality confounding. Data were normalized using term frequency-inverse document frequency (TF-IDF) transformation, dimensionality was reduced using singular value decomposition (excluding the first component, which was correlated with sequencing depth), and data were clustered and visualized using graph-based clustering and UMAP.

Cell-type labels from the paired snRNA-seq dataset were transferred to scATAC-seq nuclei using anchor-based label transfer (gene activity scores computed with GeneActivity, followed by FindTransferAnchors/TransferData in Seurat), reproducing the same 22 annotated cell populations. Peak calling was performed using the MACS2 algorithm implemented in Signac (q-value threshold <0.05), retaining the highest-enrichment peak among overlapping peaks and generating a non-redundant consensus peak set. Differential chromatin accessibility between LLIs and controls was assessed in curated regulatory peaks linked to longevity-signature and senescence/SASP genes, expressed as log2 fold-change (LLI vs. Control) as a function of −log10(FDR).

Transcription factor (TF) motif enrichment in differentially accessible peaks was assessed against the JASPAR2020 motif database (AddMotifs), and motif accessibility per nucleus and cell type (chromVAR-type z-scores) was computed using RunChromVAR (Schep et al., 2017), as implemented in Signac. Peak-to-gene linkage connected differentially accessible regulatory elements (enhancers/promoters) to putative target genes based on genomic distance and co-accessibility scores. Integration of chromatin accessibility with paired gene expression data (bulk/single-nucleus) was used to test correlations between TF motif accessibility and target-gene expression for candidate regulator-gene pairs.

Statistical analysis

All statistical analyses were performed in R (R Core Team) using RStudio, and all figures were generated in R using the ggplot2 graphics system and related packages.

Normality of continuous variables was assessed using, for example, the D'Agostino-Pearson or Shapiro-Wilk tests, and parametric (Student's t-test) or non-parametric (Mann-Whitney U/two-tailed Wilcoxon) tests were applied as appropriate for comparisons between two groups. Categorical variables were compared using Pearson's chi-square test or Fisher's exact test, as appropriate. For single-nucleus, spatial, histological, and molecular comparisons involving multiple simultaneous or panel-based tests, two-tailed Wilcoxon tests with Benjamini-Hochberg false discovery rate (FDR) correction (Benjamini and Hochberg, 1995) were used, applied within each analysis/figure panel, with adjusted p-values reported as "adjusted p" or "FDR p". Correlations between continuous variables were assessed using Spearman rank correlation coefficients (rho), with FDR correction applied to correlation matrices when multiple pairs were tested simultaneously. Differences in pseudotime distributions were tested using the two-sample Kolmogorov-Smirnov test. Sex-stratified comparisons within each study group, as well as comparisons between LLIs and controls (overall and stratified by sex), were performed as detailed for each table/figure. A sex-adjusted linear regression model was used to test whether the effect of group on residual age acceleration was independent of sex. Statistical significance was defined as a two-tailed p-value (or FDR-adjusted p-value, where indicated) <0.05.

Software and computational tools

Analyses were performed in R using the following packages/tools: Seurat (Hao et al., 2024), for processing, quality control, normalization, clustering, differential expression, and module scoring in single-nucleus and spatial transcriptomics; Harmony (Korsunsky et al., 2019), for batch integration; Monocle3 (Cao et al., 2019), for pseudotime trajectory inference; Signac (Stuart et al., 2021), for scATAC-seq processing, peak calling, and motif/chromVAR analysis (Schep et al., 2017); Cell2location (Kleshchevnikov et al., 2022), for spatial cell-type deconvolution; glmnet (Friedman et al., 2010), for elastic net/LASSO regression underlying the biological age clock and molecular longevity signature; spatstat (Baddeley and Turner, 2005; Baddeley et al., 2015), for cross-K function spatial statistics; a CellChat-type ligand-receptor coexpression framework (Jin et al., 2021), for intercellular communication scoring; and ImageJ/Fiji (Schneider et al., 2012), supplemented by QuPath (Bankhead et al., 2017) when applicable, for histological and immunohistochemical image quantification.

Declarations

CRediT authorship contribution statement

Matheus Corteletti: Conceptualization, Methodology, Investigation, Formal analysis, Data curation, Writing - Original draft, Writing - Review & Editing; **Wang Wei:** Methodology, Investigation, Validation, Writing - Review & Editing; **Giuseppe Mancini:** Methodology, Investigation, Validation, Writing - Review & Editing; **Niccolò Conti:** Investigation, Data curation, Formal analysis; **Xu Junjie:** Methodology, Investigation, Validation, Writing - Review & Editing; **Dominic Grün:** Conceptualization, Supervision, Project administration, Methodology, Writing - Review & Editing.

Conflict of interest

The authors declare no competing interests.

Funding

This work was supported by the National Key R&D Program of China (Grants 2018YFA0800501 and 2019YFA0801602, awarded to X.J.Z.). This study was also supported by the Coordenação de Aperfeiçoamento de Pessoal de Nível Superior (CAPES), Brazil, under Finance Codes 88887.960028/2024-00 and 88887.192216/2025-00.

References

1. Anselmi CV, Malovini A, Roncarati R, et al. Association of the FOXO3A locus with extreme longevity in a southern Italian centenarian study. Rejuvenation Res. 2009;12(2):95-104.
2. Antunes MV, Lazzaretti C, Gamaro GD, Linden R. Preanalytical and validation studies for the determination of malondialdehyde in human plasma through high performance liquid chromatography after derivatization with 2,4-dinitrophenylhydrazine. Rev Bras Cienc Farm. 2008;44(2):279-287. doi:10.1590/S1516-93322008000200013.
3. Atzmon G, Pollin TI, Crandall J, Tanner K, Schechter CB, Scherer PE, et al. Adiponectin levels and genotype: a potential regulator of life span in humans. J Gerontol A Biol Sci Med Sci. 2008;63(5):447-453. doi:10.1093/gerona/63.5.447.
4. Baddeley A, Rubak E, Turner R. Spatial Point Patterns: Methodology and Applications with R. London: Chapman and Hall/CRC Press; 2015.
5. Baddeley A, Turner R. spatstat: an R package for analyzing spatial point patterns. J Stat Softw. 2005;12(6):1-42.
6. Bankhead P, Loughrey MB, Fernández JA, Dombrowski Y, McArt DG, Dunne PD, et al. QuPath: open source software for digital pathology image analysis. Sci Rep. 2017;7:16878. doi:10.1038/s41598-017-17204-5.

7. Benjamini Y, Hochberg Y. Controlling the false discovery rate: a practical and powerful approach to multiple testing. J R Stat Soc Series B Stat Methodol. 1995;57(1):289-300.
8. Buege JA, Aust SD. Microsomal lipid peroxidation. Methods Enzymol. 1978;52:302-310.
9. Cao J, Spielmann M, Qiu X, Huang X, Ibrahim DM, Hill AJ, et al. The single-cell transcriptional landscape of mammalian organogenesis. Nature. 2019;566(7745):496-502.
10. Carrano AV, Natarajan AT. Considerations for population monitoring using cytogenetic techniques. International Commission for Protection against Environmental Mutagens and Carcinogens (ICPEMC) publication no. 14. Mutat Res. 1988;204(3):379-406.
11. Chien Y, Scuoppo C, Wang X, Fang X, Balgley B, Bolden JE, et al. Control of the senescence-associated secretory phenotype by NF-κB promotes senescence and enhances chemosensitivity. Genes Dev. 2011;25(20):2125-2136. doi:10.1101/gad.17276711.
12. Eastmond DA, Tucker JD. Identification of aneuploidy-inducing agents using cytokinesis-blocked human lymphocytes and an antikinetochore antibody. Environ Mol Mutagen. 1989;13(1):34-43.
13. Fenech M, Morley AA. Measurement of micronuclei in lymphocytes. Mutat Res. 1985;147(1-2):29-36.
14. Flachsbart F, Caliebe A, Kleindorp R, Blanche H, De Craen AJM, Stazi MA, et al. Association of FOXO3A variation with human longevity confirmed in German centenarians. Proc Natl Acad Sci U S A. 2009;106(8):2700-2705.
15. Franco PS, Capanema BSV, Pereira FDS, Barcia SO, Gil PR, Mazo GZ. Fragilidade e atividade física em centenários: revisão sistemática. ABCS Health Sci. 2022;47:e022307. doi:10.7322/abcshs.2021018.1747.
16. Friedman J, Hastie T, Tibshirani R. Regularization paths for generalized linear models via coordinate descent. J Stat Softw. 2010;33(1):1-22.
17. Fromm D, Zhu J, Kim W, Wei Y. Alcohol consumption and decreased serum α-Klotho, an anti-aging hormone, levels among US adult participants. Innov Aging. 2023;7(Suppl 1):1039. doi:10.1093/geroni/igad104.3175.
18. Hao Y, Stuart T, Kowalski MH, Choudhary S, Hoffman P, Hartman A, et al. Dictionary learning for integrative, multimodal and scalable single-cell analysis. Nat Biotechnol. 2024;42:293-304.
19. Jia G, Sowers JR, et al. Adipose tissue macrophages in aging-associated adipose tissue function. J Physiol Sci. 2021;71:38. doi:10.1186/s12576-021-00820-2.
20. Jin S, Guerrero-Juarez CF, Zhang L, Chang I, Ramos R, Kuan CH, et al. Inference and analysis of cell-cell communication using CellChat. Nat Commun. 2021;12:1088.
21. Kleshchevnikov V, Shmatko A, Dann E, Aivazidis A, King HW, Li T, et al. Cell2location maps fine-grained cell types in spatial transcriptomics. Nat Biotechnol. 2022;40(5):661-671.
22. Korsunsky I, Millard N, Fan J, Slowikowski K, Zhang F, Wei K, et al. Fast, sensitive and accurate integration of single-cell data with Harmony. Nat Methods. 2019;16(12):1289-1296.

23. Kurosu H, Yamamoto M, Clark JD, Pastor JV, Nandi A, Gurnani P, et al. Suppression of aging in mice by the hormone Klotho. Science. 2005;309(5742):1829-1833. doi:10.1126/science.1112766.
24. Meyer DH, Schumacher B. BiT age: a transcriptome-based aging clock near the theoretical limit of accuracy. Aging Cell. 2021;20(3):e13320. doi:10.1111/acel.13320.
25. Miller SA, Dykes DD, Polesky HF. A simple salting out procedure for extracting DNA from human nucleated cells. Nucleic Acids Res. 1988;16(3):1215.
26. Orta T, Günebakan S. The effect of aging on micronuclei frequency and proliferation in human peripheral blood lymphocytes. Indian J Hum Genet. 2012;18(1):95-100. doi:10.4103/0971-6866.96671.
27. Palla G, Spitzer H, Klein M, Fischer D, Schaar AC, Kuemmerle LB, et al. Squidpy: a scalable framework for spatial omics analysis. Nat Methods. 2022;19(2):171-178.
28. Schep AN, Wu B, Buenrostro JD, Greenleaf WJ. chromVAR: inferring transcription-factor-associated accessibility from single-cell epigenomic data. Nat Methods. 2017;14(10):975-978.
29. Schneider CA, Rasband WS, Eliceiri KW. NIH Image to ImageJ: 25 years of image analysis. Nat Methods. 2012;9(7):671-675.
30. Stuart T, Srivastava A, Madad S, Lareau CA, Satija R. Single-cell chromatin state analysis with Signac. Nat Methods. 2021;18(11):1333-1341.
31. Thomas P, Holland N, Bolognesi C, Kirsch-Volders M, Bonassi S, Zeiger E, et al. Buccal micronucleus cytome assay. Nat Protoc. 2009;4(6):825-837.
32. Tian T, Liu M, Little PJ, Strijdom H, Weng J, Xu S. Emerging roles of GDF15 in metabolic and cardiovascular diseases. Research (Wash DC). 2025. doi:10.34133/research.0832.
33. Tsikas D, Tsikas SA, Mikuteit M, Ückert S. Circulating and urinary concentrations of malondialdehyde in aging humans in health and disease: review and discussion. Biomedicines. 2023;11(10):2744. doi:10.3390/biomedicines11102744.
34. Ware JE Jr, Sherbourne CD. The MOS 36-item short-form health survey (SF-36). I. Conceptual framework and item selection. Med Care. 1992;30(6):473-483.
35. Whytock KL, Divoux A, Sun Y, Pino MF, Yu G, Jin CA, et al. Aging human abdominal subcutaneous white adipose tissue at single cell resolution. Aging Cell. 2024;23(11):e14287. doi:10.1111/acel.14287.
36. Willcox BJ, Donlon TA, He Q, Chen R, Grove JS, Yano K, et al. FOXO3A genotype is strongly associated with human longevity. Proc Natl Acad Sci U S A. 2008;105(37):13987-13992. doi:10.1073/pnas.0801030105.
37. Wojda A, Zietkiewicz E, Witt M. Effects of age and gender on micronucleus and chromosome nondisjunction frequencies in centenarians and younger subjects. Mutagenesis. 2007;22(3):195-200.
38. Zoico E, Rubele S, De Caro A, Nori N, Mazzali G, Fantin F, et al. Brown and beige adipose tissue and aging. Front Endocrinol (Lausanne). 2019;10:368. doi:10.3389/fendo.2019.00368.

39. dos Santos MC, da Silva DS, Cordeiro JP, Domingos LF, da Silva Gomes EH, Nogueira BV, et al. High-intensity interval training improves cardiomyocyte contractile function and myofilament sensitivity to intracellular Ca2+ in obese rats. Exp Physiol. 2024;109(10):1710-1727. doi:10.1113/EP092015.

Tables

Table 1: Sociodemographic and lifestyle characteristics

Variable	Total (n = 210)	Long-lived (n = 140)	Controls (n = 70)	p-value
Sociodemographic characteristics				
Age, years, mean ± SD	84.8 ± 9.7	90.9 ± 5.2	72.5 ± 1.4	<0.001
Sex, n (%)				0.528
Male	66 (31.4%)	42 (30.0%)	24 (34.3%)	
Female	144 (68.6%)	98 (70.0%)	46 (65.7%)	
Race/skin color, n (%)				0.940
White/Caucasian	89 (42.4%)	59 (42.1%)	30 (42.9%)	
Black	21 (10.0%)	15 (10.7%)	6 (8.6%)	
Mixed-race (Pardo)	35 (16.7%)	24 (17.1%)	11 (15.7%)	
Italian ancestry	65 (31.0%)	42 (30.1%)	23 (32.8%)	
Marital status, n (%)				<0.001
Married	71 (33.8%)	36 (25.7%)	35 (50.0%)	
Widowed	103 (49.0%)	81 (57.9%)	22 (31.4%)	
Separated/Divorced/Single	36 (17.1%)	23 (16.4%)	13 (18.6%)	
Educational level, n (%)				0.672
0 years	18 (8.6%)	14 (10.0%)	4 (5.7%)	
1–4 years	115 (54.8%)	76 (54.3%)	39 (55.7%)	
5–8 years	73 (34.8%)	48 (34.3%)	25 (35.7%)	
>8 years	4 (1.9%)	2 (1.4%)	2 (2.9%)	
Monthly income ≤2 minimum wages, n (%)	106 (50.5%)	71 (50.7%)	35 (50.0%)	0.920
Housing type, n (%)				0.265

Variable	Total (n = 210)	Long-lived (n = 140)	Controls (n = 70)	p-value
Own home	188 (89.5%)	123 (87.9%)	65 (92.9%)	
Rented/Living with others	22 (10.5%)	17 (12.1%)	5 (7.1%)	
Lifestyle characteristics				
Smoking status, n (%)				0.590
Never smoker	136 (64.8%)	94 (67.1%)	42 (60.0%)	
Former smoker	63 (30.0%)	39 (27.9%)	24 (34.3%)	
Current smoker	11 (5.2%)	7 (5.0%)	4 (5.7%)	
Alcohol consumption, n (%)				0.018
Alcohol consumer	21 (10.0%)	9 (6.4%)	12 (17.1%)	
Physical activity, n (%)				0.003
Physically active	44 (21.0%)	21 (15.0%)	23 (32.9%)	
Vegetable consumption ≥5×/week, n (%)	179 (85.2%)	121 (86.4%)	58 (82.9%)	0.502
Fruit consumption ≥5×/week, n (%)	184 (87.6%)	125 (89.3%)	59 (84.3%)	0.321

Table 1. Sociodemographic and lifestyle characteristics of long-lived individuals and controls. Data are presented as mean ± standard deviation (SD) for continuous variables and as absolute numbers (n) and percentages (%) for categorical variables. Comparisons were performed between long-lived individuals and controls. $p < 0.05$ was considered statistically significant.

Table 2: Clinical, anthropometric, medical history, biochemical, and biomarker characteristics

Characteristics	Long-lived individuals		p†	Controls		p†	p‡
	Men (n=42)	Women (n=98)		Men (n=24)	Women (n=46)		
Clinical and anthropometric characteristics							
Age, years	90.1 ± 5.0	91.2 ± 7.3	0.286	72.4 ± 1.5	72.6 ± 1.4	0.612	<0.001
BMI, kg/m²	27.1 ± 6.1	26.9 ± 4.6	0.818	27.6 ± 4.7	27.7 ± 5.1	0.954	0.308
Waist circumference, cm	96.8 ± 13.8	91.5 ± 10.8	0.021	97.3 ± 9.0	93.2 ± 10.4	0.123	0.337
Hip circumference, cm	100.2 ± 9.3	102.2 ± 8.6	0.247	101.2 ± 6.6	103.0 ± 9.6	0.438	0.530
Waist-to-hip ratio	1.0 ± 0.1	0.9 ± 0.1	0.005	1.0 ± 0.1	0.9 ± 0.1	0.114	0.610
Body fat, %	29.5 ± 8.6	36.6 ± 8.3	<0.001	26.0 ± 6.2	37.5 ± 8.2	<0.001	0.558
Subscapular skinfold, mm	22.7 ± 6.2	21.5 ± 7.2	0.415	18.8 ± 7.8	21.6 ± 7.7	0.163	0.334
Systolic blood pressure, mmHg	137.4 ± 17.4	129.6 ± 15.8	0.015	137.4 ± 14.2	129.8 ± 17.7	0.083	0.826
Diastolic blood pressure, mmHg	79.6 ± 8.5	79.2 ± 9.6	0.839	78.5 ± 8.9	83.2 ± 10.2	0.075	0.078
Medical history							
Hypertension, n (%)	10 (28.6)	43 (41.0)	0.268	7 (33.3)	23 (46.9)	0.429	0.583
Diabetes mellitus, n (%)	11 (31.4)	24 (22.9)	0.430	2 (9.5)	10 (20.4)	0.447	0.266
Neurodegenerative disease, n (%)	4 (11.4)	13 (12.4)	1.000	10 (47.6)	19 (38.8)	0.672	<0.001
Neoplasm, n (%)	7 (20.0)	22 (21.0)	1.000	7 (33.3)	6 (12.2)	0.081	0.855
Respiratory disease, n (%)	7 (20.0)	23 (21.9)	1.000	3 (14.3)	9 (18.4)	0.945	0.583
Blood biochemistry							

Characteristics	Long-lived individuals		p†	Controls		p†	p‡
Hemoglobin, g/dL	14.1 ± 1.8	13.1 ± 1.2	<0.001	14.7 ± 1.4	13.1 ± 1.1	<0.001	0.320
Hematocrit, %	44.8 ± 3.8	40.4 ± 4.1	<0.001	44.6 ± 4.2	40.9 ± 4.2	0.001	0.446
Leukocytes, ×10³/µL	7.0 ± 2.3	7.0 ± 1.7	0.940	7.6 ± 2.1	6.8 ± 1.7	0.108	0.756
Neutrophils, %	59.5 ± 9.3	57.9 ± 6.9	0.289	57.1 ± 6.6	57.1 ± 7.8	0.997	0.258
Lymphocytes, %	32.6 ± 9.1	34.4 ± 7.2	0.249	35.1 ± 7.0	34.9 ± 9.0	0.937	0.364
Platelets, ×10³/µL	250.6 ± 52.9	234.5 ± 55.3	0.133	243.0 ± 43.6	238.4 ± 59.1	0.751	0.880
Fasting glucose, mg/dL	98.3 ± 17.1	103.2 ± 26.6	0.302	96.7 ± 20.0	98.4 ± 24.1	0.770	0.246
HbA1c, %	5.6 ± 0.9	5.6 ± 0.8	0.879	5.6 ± 0.6	5.7 ± 0.8	0.567	0.583
Insulin, µIU/mL	9.5 ± 8.6	10.6 ± 9.0	0.543	9.1 ± 6.3	11.6 ± 9.5	0.282	0.698
HOMA-IR	2.5 ± 2.4	2.9 ± 2.9	0.401	2.3 ± 1.7	3.1 ± 3.1	0.248	0.898
Total cholesterol, mg/dL	196.2 ± 35.0	182.5 ± 35.4	0.049	174.8 ± 36.8	190.9 ± 42.5	0.135	0.979
LDL-C, mg/dL	103.4 ± 29.5	108.8 ± 29.9	0.353	111.3 ± 27.8	113.5 ± 34.5	0.798	0.238
HDL-C, mg/dL	49.2 ± 12.7	56.2 ± 14.7	0.013	47.9 ± 15.9	56.4 ± 15.4	0.039	0.775
Triglycerides, mg/dL	139.2 ± 60.6	131.5 ± 56.5	0.494	130.2 ± 67.7	132.9 ± 64.2	0.877	0.879
AST, U/L	24.1 ± 8.7	23.5 ± 8.3	0.702	26.2 ± 7.9	22.3 ± 8.3	0.076	0.880
ALT, U/L	20.6 ± 9.7	21.8 ± 9.8	0.513	20.5 ± 9.5	22.6 ± 10.1	0.435	0.776
Creatinine, mg/dL	1.1 ± 0.3	0.9 ± 0.2	<0.001	1.0 ± 0.2	0.9 ± 0.2	0.004	0.952
Urea, mg/dL	34.2 ± 10.6	35.1 ± 10.0	0.641	33.0 ± 13.8	36.3 ± 9.8	0.264	0.762
Albumin, g/dL	4.1 ± 0.3	4.1 ± 0.4	0.437	4.0 ± 0.3	4.2 ± 0.4	0.020	0.278
hs-CRP, mg/L	4.8 ± 10.4	5.3 ± 7.6	0.758	4.9 ± 8.6	3.6 ± 7.1	0.533	0.328

Characteristics	Long-lived individuals		p†	Controls		p†	p‡
Ferritin, ng/mL	165.4 ± 72.2	86.4 ± 59.2	<0.001	152.3 ± 75.9	92.4 ± 63.4	0.001	0.687
Fibrinogen, mg/dL	322.5 ± 61.0	312.0 ± 62.2	0.390	324.0 ± 38.8	313.1 ± 59.7	0.445	0.842
NT-proBNP, pg/mL	250.0 ± 496.5	204.1 ± 246.4	0.472	159.0 ± 163.2	161.2 ± 272.0	0.973	0.213
hs-Troponin I, ng/L	8.5 ± 8.2	9.2 ± 9.6	0.705	6.5 ± 5.2	4.5 ± 3.9	0.088	<0.001
Vitamin D, ng/mL	25.3 ± 11.3	25.2 ± 10.6	0.961	26.7 ± 13.2	28.9 ± 10.9	0.467	0.059
Vitamin B12, pg/mL	432.0 ± 154.1	423.5 ± 140.3	0.763	379.5 ± 130.3	412.2 ± 155.0	0.400	0.275
Folate, ng/mL	9.8 ± 3.8	9.7 ± 4.0	0.887	9.6 ± 4.5	9.5 ± 3.6	0.964	0.743
Homocysteine, µmol/L	12.4 ± 4.0	11.8 ± 4.6	0.462	10.7 ± 4.2	10.6 ± 3.4	0.879	0.027
ELISA biomarkers							
IL-6, pg/mL	3.8 ± 6.6	5.5 ± 7.9	0.248	7.1 ± 12.5	3.2 ± 2.9	0.041	0.515
TNF-α, pg/mL	5.0 ± 4.9	5.5 ± 4.4	0.572	5.0 ± 5.9	3.4 ± 2.6	0.123	0.017
IL-1β, pg/mL	2.2 ± 2.6	2.0 ± 2.0	0.629	1.9 ± 2.2	1.4 ± 1.5	0.280	0.101
MCP-1/CCL2, pg/mL	281.0 ± 125.8	297.7 ± 118.9	0.479	221.4 ± 115.2	275.3 ± 120.5	0.087	0.052
TGF-β1, pg/mL	27,612.7 ± 8,300.1	28,381.2 ± 7,913.3	0.624	23,745.6 ± 7,275.8	26,252.3 ± 7,096.5	0.183	0.018
GDF-15, pg/mL	1,849.9 ± 2,147.2	1,527.5 ± 1,756.9	0.376	1,789.9 ± 2,241.1	962.5 ± 906.1	0.030	0.120
PAI-1, ng/mL	34.9 ± 23.6	37.3 ± 19.3	0.536	32.6 ± 16.3	34.4 ± 23.5	0.751	0.355
Klotho, pg/mL	666.7 ± 195.4	619.6 ± 229.2	0.278	562.5 ± 312.6	770.3 ± 232.4	0.003	0.030
FGF-21, pg/mL	268.5 ± 251.4	255.9 ± 232.7	0.786	202.0 ± 138.6	205.5 ± 163.0	0.931	0.082
IGF-1, ng/mL	143.1 ± 51.6	138.0 ± 54.3	0.626	139.5 ± 61.5	150.2 ± 52.6	0.459	0.331

Characteristics	Long-lived individuals		p†	Controls		p†	p‡
Adiponectin, µg/mL	8.1 ± 4.9	11.3 ± 5.2	0.002	8.4 ± 5.1	11.0 ± 5.4	0.056	0.757
Leptin, ng/mL	12.9 ± 12.9	20.1 ± 18.0	0.031	8.8 ± 9.5	18.5 ± 16.4	0.014	0.271
NfL, pg/mL	26.7 ± 33.1	21.3 ± 22.0	0.275	16.9 ± 19.9	17.5 ± 16.6	0.897	0.110
MPO, ng/mL	38.2 ± 18.1	39.4 ± 17.0	0.725	37.9 ± 24.1	30.6 ± 18.2	0.167	0.018

Table 2. Clinical, anthropometric, medical history, biochemical, and biomarker characteristics of long-lived individuals and controls, stratified by sex. Data are presented as mean ± standard deviation (SD) for continuous variables and as absolute numbers (n) and percentages (%) for categorical variables. The †*p*-value represents comparisons between men and women within each study group, whereas the ‡*p*-value represents comparisons between long-lived individuals and controls. A *p*-value < 0.05 was considered statistically significant. **LLI**, long-lived individuals; **BMI**, body mass index; **SBP**, systolic blood pressure; **DBP**, diastolic blood pressure; **WHR**, waist-to-hip ratio; **HbA1c**, glycated hemoglobin; **HOMA-IR**, homeostatic model assessment of insulin resistance; **LDL-C**, low-density lipoprotein cholesterol; **HDL-C**, high-density lipoprotein cholesterol; **AST**, aspartate aminotransferase; **ALT**, alanine aminotransferase; **hs-CRP**, high-sensitivity C-reactive protein; **NT-proBNP**, N-terminal pro-B-type natriuretic peptide; **hs-Troponin I**, high-sensitivity cardiac troponin I; **NfL**, neurofilament light chain; **MPO**, myeloperoxidase. †*p*-value for comparisons between men and women within each study group. ‡*p*-value for comparison between long-lived individuals and controls. Bold values indicate statistical significance ($p < 0.05$)

Table 3: Cytogenetic damage and plasma oxidative stress biomarkers in long-lived individuals and controls

Characteristics	Long-lived individuals (n=140)	Controls (n=70)	p‡
Cytogenetic damage parameters			
CBMNcyt assay – Peripheral blood lymphocytes			
Micronuclei (MN/1,000 cells)	**7.8 ± 2.6**	**11.4 ± 3.2**	<0.001
Nucleoplasmic bridges (NPB/1,000 cells)	**0.6 ± 0.2**	**1.4 ± 0.6**	<0.001
Nuclear buds (NBUD/1,000 cells)	**1.9 ± 0.9**	**3.9 ± 1.8**	<0.001
Nuclear division index (NDI)	2.0 ± 0.2	1.9 ± 0.8	0.214
BMNcyt assay – Buccal epithelial cells			
Micronuclei (MN/1,000 cells)	**3.2 ± 1.5**	**4.9 ± 1.5**	<0.001
Nuclear buds (NBUD/1,000 cells)	**0.7 ± 0.5**	**2.5 ± 1.3**	<0.001
Binucleated cells/1,000 cells	**12.1 ± 3.4**	**26.8 ± 14.9**	<0.001
Condensed chromatin/1,000 cells	**33.9 ± 21.2**	**65.1 ± 24.8**	<0.001
Karyorrhexis/1,000 cells	**17.1 ± 15.1**	**31.9 ± 17.2**	<0.001
Karyolysis/1,000 cells	169.4 ± 125.3	281.2 ± 138.5	<0.001
Pyknotic cells/1,000 cells	**2.6 ± 1.1**	**4.1 ± 1.3**	<0.001
Plasma oxidative stress biomarker			
Malondialdehyde (MDA), µmol/L	**0.46 ± 0.15**	**0.56 ± 0.16**	**0.033**

Table 3. Cytogenetic damage and plasma oxidative stress biomarkers in long-lived individuals and controls. Data are presented as mean ± standard deviation (SD). CBMNcyt, cytokinesis-block micronucleus cytome assay; BMNcyt, buccal micronucleus cytome assay; MN, micronuclei; NPB, nucleoplasmic bridges; NBUD, nuclear buds; NDI, nuclear division index; MDA, malondialdehyde. The *p*‡ value indicates the comparison between long-lived individuals and controls. Statistical significance was defined as $p < 0.05$.

Figures

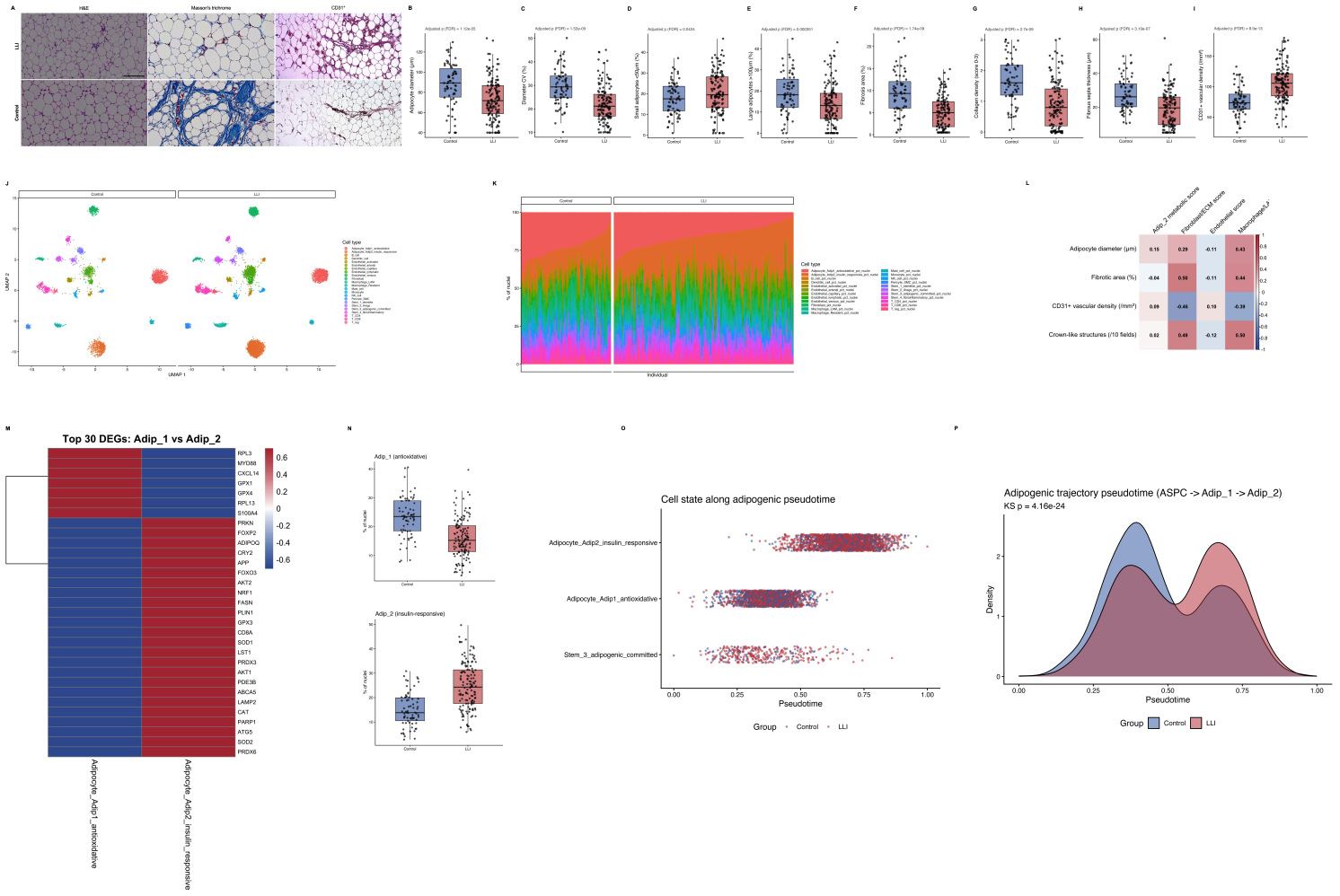


Figure 1

Histological remodeling, cellular composition, and adipogenic differentiation of subcutaneous adipose tissue in long-lived individuals. (A) Representative H&E, Masson's trichrome, and CD31 immunohistochemistry images of subcutaneous adipose tissue from Control and long-lived individuals (LLI). Scale bars, 100 µm. (B–I) Quantitative histological assessment of adipose tissue morphology and extracellular matrix remodeling, including adipocyte diameter (B), adipocyte diameter coefficient of variation (C), proportion of small adipocytes (<50 µm) (D), proportion of large adipocytes (>100 µm) (E), fibrotic area (F), collagen density score (G), fibrous septa thickness (H), and CD31⁺vascular density (I). (J) Integrated single-nucleus RNA-sequencing UMAP showing the 22 annotated cell types identified across subcutaneous adipose tissue samples from Control and LLI. (K) Per-individual cellular composition, showing the relative proportion of each of the 22 cell types in Control and LLI samples. (L) Spearman correlation matrix integrating histological parameters with matched transcriptional module scores, including adipocyte diameter with the Adip_2 metabolic score, fibrotic area with the Fibroblast/ECM score, CD31⁺vascular density with the Endothelial score, and crown-like structure density with the Macrophage/LAM score. (M) Heatmap of the top 30 differentially expressed genes between the Adip_1 and Adip_2 adipocyte subtypes. (N) Relative abundance of the Adip_1 (antioxidative) and Adip_2 (insulin-responsive) adipocyte subtypes in Control and LLI. (O) Adipogenic differentiation

trajectory reconstructed by pseudotime analysis, showing the progression from adipose-derived stem/progenitor cells (ASPC/Stem_3) through Adip_1 to Adip_2 states. (P) Density distribution of adipogenic pseudotime values in Control and LLI, with the group difference assessed using the Kolmogorov–Smirnov test. Boxplots show median, interquartile range (IQR), and 1.5×IQR whiskers, with individual data points overlaid. Correlations were assessed using Spearman's rank correlation and false discovery rate (FDR) correction where indicated. Group comparisons were performed using two-sided Wilcoxon rank-sum tests with Benjamini–Hochberg FDR correction. Control, n = 70; LLI (long-lived individuals), n = 140.

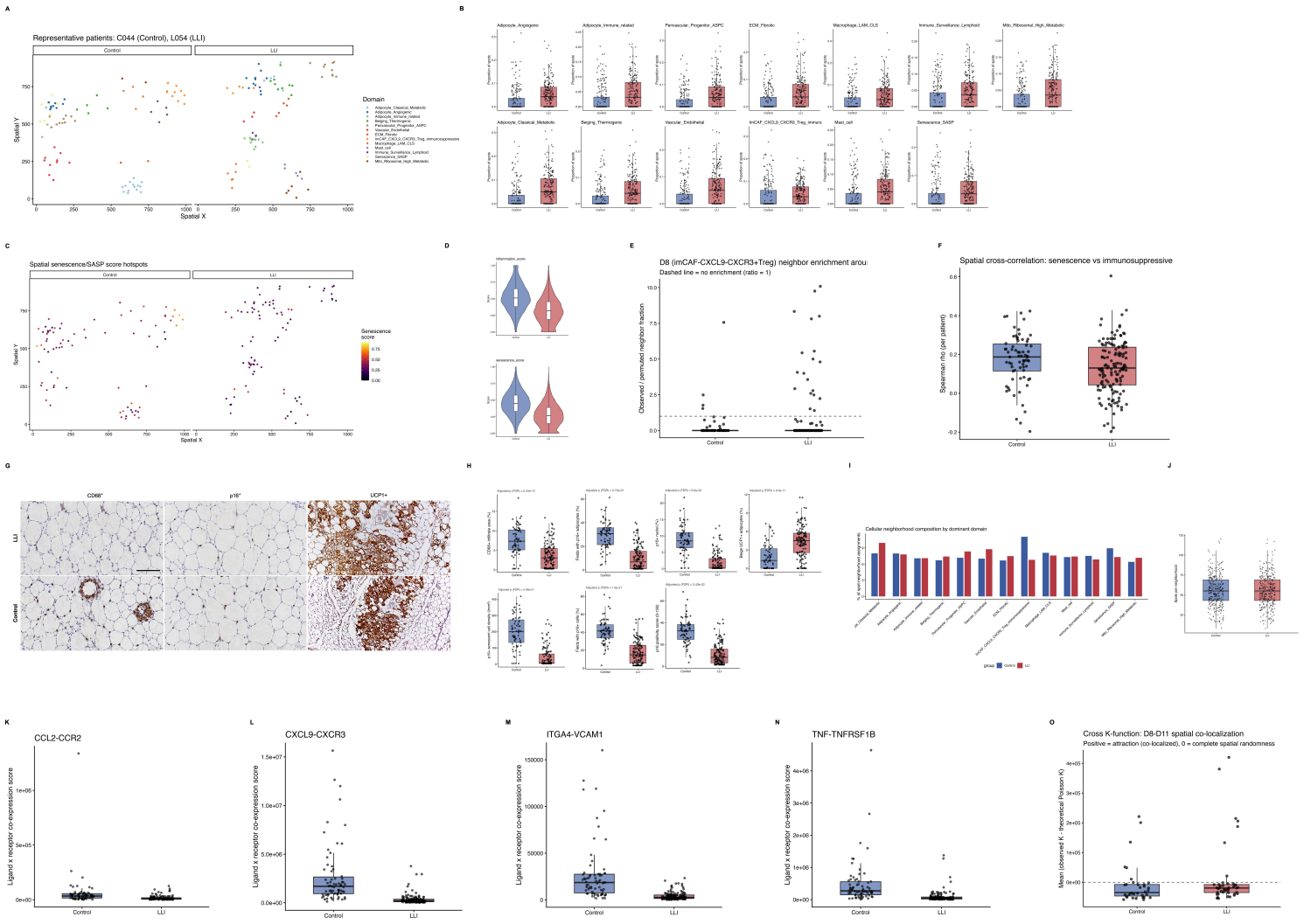


Figure 2

Spatial organization of senescence, immune niches, and cellular communication in subcutaneous adipose tissue.(A) Representative spatial domain maps of one Control (C044) and one long-lived (L054) individual, showing the 13 canonical spatial domains identified across the cohort. (B) Per-patient proportion of spots assigned to each of the 13 spatial domains, compared between Control and LLI. (C) Spatial mapping of the senescence/SASP score onto tissue coordinates for the same representative patients shown in (A). (D) Violin plots of the inflammation score and senescence score per spot, by group. (E) Neighbor enrichment of the D8 (imCAF-CXCL9-CXCR3⁺Treg immunosuppressive) domain

around senescent spots, expressed as the ratio of observed to permuted neighbor fraction; the dashed line indicates no enrichment (ratio = 1). (F) Per-patient Spearman correlation (rho) between the senescence score and the immunosuppressive score across spatial coordinates. (G) Representative CD68, p16, and UCP1 immunohistochemistry images from Control and LLI subcutaneous adipose tissue. Scale bars, 100 μm. (H) Quantification of the images in (G): $CD68^{+}$infiltrate area, $p16^{+}$ senescent cell density, fields with $p16^{+}$cells, fields with $p16^{+}$ adipocytes, $p16^{+}$ nuclei, p16 positivity score, and beige $UCP1^{+}$ adipocyte proportion. (I) Cellular neighborhood composition, expressed as the percentage of spot-neighborhood assignments dominated by each spatial domain, by group. (J) Number of spots per neighborhood, by group. (K–N) Ligand-receptor co-expression scores for the CCL2-CCR2, CXCL9-CXCR3, ITGA4-VCAM1, and TNF-TNFRSF1B axes, by group. (O) Cross K-function analysis of D8-D11 (imCAF-CXCL9-$CXCR3^{+}$Treg / Senescence-SASP) spatial co-localization, expressed as the mean difference between observed and theoretical Poisson K values; positive values indicate spatial attraction (co-localization), and the dashed line indicates complete spatial randomness. Boxplots show median, interquartile range (IQR), and 1.5×IQR whiskers, with individual data points overlaid. Group comparisons were performed using two-sided Wilcoxon rank-sum tests, with Benjamini-Hochberg false discovery rate (FDR) correction applied across all comparisons within each panel where indicated. Control, n = 70; LLI (long-lived individuals), n = 140.

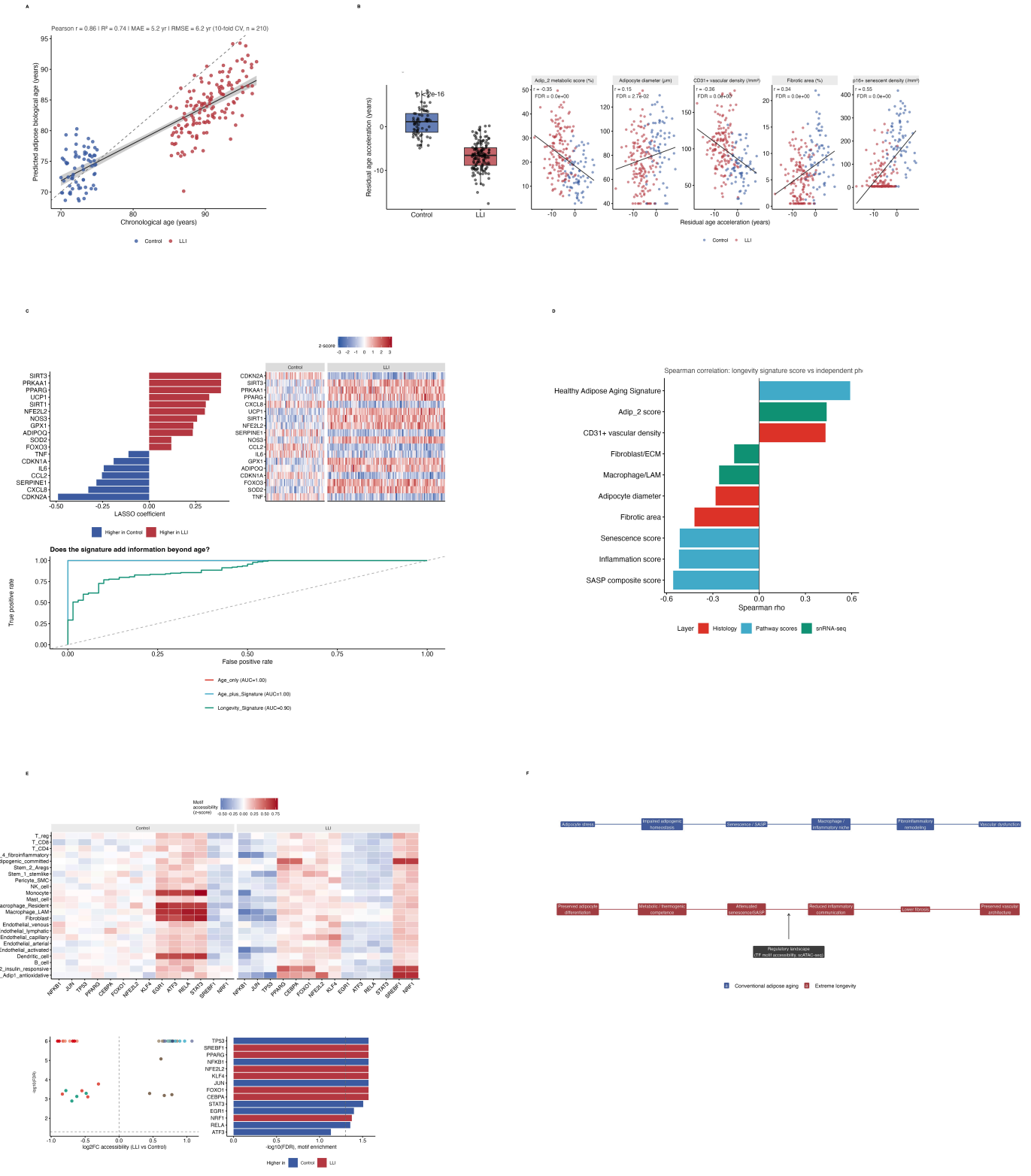


Figure 3

Reduced adipose biological aging and a molecular-regulatory signature of extreme longevity. (A) Predicted adipose biological age versus chronological age, derived from an elastic net/LASSO model trained on bulk adipose RNA-seq (10-fold cross-validation, n = 210); Pearson r, R^2, mean absolute error (MAE), and root-mean-square error (RMSE) are shown. The dashed line indicates the identity line (predicted = chronological age); the solid line and shaded band show the fitted regression with 95%

confidence interval, by group. (B) Residual age acceleration (predicted minus chronological age, adjusted for chronological age), compared between Control and LLI (left), and its correlation with the Adip_2 metabolic score, adipocyte diameter, $CD31^+$ vascular density, fibrotic area, and $p16^+$ senescent cell density (right five panels); Spearman's rho and false discovery rate (FDR)-adjusted p-values are shown in each panel. (C) LASSO coefficients of the age-adjusted adipose longevity molecular signature, with genes ranked by coefficient magnitude and colored by direction (higher in Control vs. higher in LLI); heatmap showing z-scored expression of the signature genes across all samples, ordered by group; and receiver operating characteristic (ROC) curves comparing an age-only model, an age-plus-signature model, and the longevity signature alone, with area under the curve (AUC) indicated for each model. (D) Spearman correlation (rho) between the individual-level longevity signature score and independent phenotypic layers, including histological parameters (adipocyte diameter, fibrotic area, $CD31^+$ vascular density), single-nucleus RNA-sequencing module scores (Adip_2 score, Fibroblast/ECM, Macrophage/LAM), and spatial pathway scores (senescence, inflammation, SASP composite, Healthy Adipose Aging Signature). (E) scATAC-seq regulatory architecture of the longevity signature: transcription-factor (TF) motif accessibility (z-score) across the 22 annotated cell populations, by group; differential chromatin accessibility of curated regulatory peaks ($\log_2$ fold-change, LLI vs. Control) plotted against $-\log_{10}$(FDR), colored by the direction of enrichment; and TF motif enrichment among differentially accessible peaks, ranked by $-\log_{10}$(FDR) and colored by the group in which each motif is more accessible. (F) Integrated conceptual model contrasting conventional adipose aging (adipocyte stress → impaired adipogenic homeostasis → senescence/SASP → macrophage/inflammatory niche → fibroinflammatory remodeling → vascular dysfunction) with extreme longevity (preserved adipocyte differentiation → metabolic/thermogenic competence → attenuated senescence/SASP → reduced inflammatory communication → lower fibrosis → preserved vascular architecture), with the scATAC-seq-derived regulatory landscape (TF motif accessibility) positioned as the regulatory layer supporting the attenuated senescence/SASP node of the longevity trajectory. Boxplots show median, interquartile range (IQR), and 1.5×IQR whiskers, with individual data points overlaid. Group comparisons were performed using two-sided Wilcoxon rank-sum tests, with Benjamini-Hochberg FDR correction applied across all comparisons within each panel where indicated. Control, n = 70; LLI (long-lived individuals), n = 140.

Supplementary Files

This is a list of supplementary files associated with this preprint. Click to download.

- SuplementarfigureS1.jpeg
- SuplementarfigureS2.jpeg
- SuplementarFigure3.jpeg